The Astrophysical Journal, 722:520–542, 2010 October 10 doi:10.1088/0004-637X/722/1/520

GAMMA-RAY LIGHT CURVES AND VARIABILITY OF BRIGHT *FERMI*-DETECTED BLAZARS

A. A. Abdo[1,2], M. Ackermann[3], M. Ajello[3], E. Antolini[4,5], L. Baldini[6], J. Ballet[7], G. Barbiellini[8,9], D. Bastieri[10,11], K. Bechtol[3], R. Bellazzini[6], B. Berenji[3], R. D. Blandford[3], E. D. Bloom[3], E. Bonamente[4,5], A. W. Borgland[3], A. Bouvier[3], J. Bregeon[6], A. Brez[6], M. Brigida[12,13], P. Bruel[14], R. Buehler[3], T. H. Burnett[15], S. Buson[10], G. A. Caliandro[16], R. A. Cameron[3], P. A. Caraveo[17], S. Carrigan[11], J. M. Casandjian[7], E. Cavazzuti[18], C. Cecchi[4,5], Ö. Çelik[19,20,21], A. Chekhtman[1,22], C. C. Cheung[1,2], J. Chiang[3], S. Ciprini[5,58], R. Claus[3], J. Cohen-Tanugi[23], L. R. Cominsky[24], J. Conrad[25,26,56], L. Costamante[3], S. Cutini[18], C. D. Dermer[1], A. de Angelis[27], F. de Palma[12,13], E. do Couto e Silva[3], P. S. Drell[3], R. Dubois[3], D. Dumora[28,29], C. Farnier[23], C. Favuzzi[12,13], S. J. Fegan[14], W. B. Focke[3], P. Fortin[14], M. Frailis[27,30], Y. Fukazawa[31], S. Funk[3], P. Fusco[12,13], F. Gargano[13], D. Gasparrini[18], N. Gehrels[19], S. Germani[4,5], B. Giebels[14], N. Giglietto[12,13], P. Giommi[18], F. Giordano[12,13], T. Glanzman[3], G. Godfrey[3], I. A. Grenier[7], M.-H. Grondin[28,29], J. E. Grove[1], S. Guiriec[32], D. Hadasch[33], M. Hayashida[3], E. Hays[19], S. E. Healey[3], D. Horan[14], R. E. Hughes[34], R. Itoh[31], G. Jóhannesson[3], A. S. Johnson[3], W. N. Johnson[1], T. Kamae[3], H. Katagiri[31], J. Kataoka[35], N. Kawai[36,37], J. Knödlseder[38], M. Kuss[6], J. Lande[3], S. Larsson[25,26,39], L. Latronico[6], M. Lemoine-Goumard[28,29], F. Longo[8,9], F. Loparco[12,13], B. Lott[28,29], M. N. Lovellette[1], P. Lubrano[4,5], G. M. Madejski[3], A. Makeev[1,22], E. Massaro[40], M. N. Mazziotta[13], J. E. McEnery[19,41], P. F. Michelson[3], W. Mitthumsiri[3], T. Mizuno[31], A. A. Moiseev[20,41], C. Monte[12,13], M. E. Monzani[3], A. Morselli[42], I. V. Moskalenko[3], M. Mueller[3], S. Murgia[3], P. L. Nolan[3], J. P. Norris[43], E. Nuss[23], M. Ohno[44], T. Ohsugi[45], N. Omodei[3], E. Orlando[46], J. F. Ormes[43], M. Ozaki[44], J. H. Panetta[3], D. Parent[1,22,28,29], V. Pelassa[23], M. Pepe[4,5], M. Pesce-Rollins[6], F. Piron[23], T. A. Porter[3], S. Rainò[12,13], R. Rando[10,11], M. Razzano[6], A. Reimer[47,3], O. Reimer[47,3], S. Ritz[48], A. Y. Rodriguez[16], R. W. Romani[3], M. Roth[15], F. Ryde[26,49], H. F.-W. Sadrozinski[48], A. Sander[34], J. D. Scargle[50], C. Sgrò[6], M. S. Shaw[3], P. D. Smith[34], G. Spandre[6], P. Spinelli[12,13], J.-L. Starck[7], M. S. Strickman[1], D. J. Suson[51], H. Takahashi[45], T. Takahashi[44], T. Tanaka[3], J. B. Thayer[3], J. G. Thayer[3], D. J. Thompson[19], L. Tibaldo[10,11,7,57], D. F. Torres[33,16], G. Tosti[4,5], A. Tramacere[3,52,53], Y. Uchiyama[3], T. L. Usher[3], V. Vasileiou[20,21], N. Vilchez[38], V. Vitale[42,54], A. P. Waite[3], E. Wallace[15], P. Wang[3], B. L. Winer[34], K. S. Wood[1], Z. Yang[25,26], T. Ylinen[26,49,55], and M. Ziegler[48]

[1] Space Science Division, Naval Research Laboratory, Washington, DC 20375, USA
[2] National Research Council Research Associate, National Academy of Sciences, Washington, DC 20001, USA
[3] W. W. Hansen Experimental Physics Laboratory, Kavli Institute for Particle Astrophysics and Cosmology, Department of Physics and SLAC National Accelerator Laboratory, Stanford University, Stanford, CA 94305, USA
[4] Istituto Nazionale di Fisica Nucleare, Sezione di Perugia, I-06123 Perugia, Italy; Gino.Tosti@pg.infn.it.
[5] Dipartimento di Fisica, Università degli Studi di Perugia, I-06123 Perugia, Italy; stefano.ciprini@pg.infn.it
[6] Istituto Nazionale di Fisica Nucleare, Sezione di Pisa, I-56127 Pisa, Italy
[7] Laboratoire AIM, CEA-IRFU/CNRS/Université Paris Diderot, Service d'Astrophysique, CEA Saclay, 91191 Gif sur Yvette, France
[8] Istituto Nazionale di Fisica Nucleare, Sezione di Trieste, I-34127 Trieste, Italy
[9] Dipartimento di Fisica, Università di Trieste, I-34127 Trieste, Italy
[10] Istituto Nazionale di Fisica Nucleare, Sezione di Padova, I-35131 Padova, Italy
[11] Dipartimento di Fisica "G. Galilei," Università di Padova, I-35131 Padova, Italy
[12] Dipartimento di Fisica "M. Merlin" dell'Università e del Politecnico di Bari, I-70126 Bari, Italy
[13] Istituto Nazionale di Fisica Nucleare, Sezione di Bari, 70126 Bari, Italy
[14] Laboratoire Leprince-Ringuet, École polytechnique, CNRS/IN2P3, Palaiseau, France
[15] Department of Physics, University of Washington, Seattle, WA 98195-1560, USA
[16] Institut de Ciencies de l'Espai (IEEC-CSIC), Campus UAB, 08193 Barcelona, Spain
[17] INAF-Istituto di Astrofisica Spaziale e Fisica Cosmica, I-20133 Milano, Italy
[18] Agenzia Spaziale Italiana (ASI) Science Data Center, I-00044 Frascati (Roma), Italy; sarac@slac.stanford.edu
[19] NASA Goddard Space Flight Center, Greenbelt, MD 20771, USA
[20] Center for Research and Exploration in Space Science and Technology (CRESST) and NASA Goddard Space Flight Center, Greenbelt, MD 20771, USA
[21] Department of Physics and Center for Space Sciences and Technology, University of Maryland Baltimore County, Baltimore, MD 21250, USA
[22] George Mason University, Fairfax, VA 22030, USA
[23] Laboratoire de Physique Théorique et Astroparticules, Université Montpellier 2, CNRS/IN2P3, Montpellier, France
[24] Department of Physics and Astronomy, Sonoma State University, Rohnert Park, CA 94928-3609, USA
[25] Department of Physics, Stockholm University, AlbaNova, SE-106 91 Stockholm, Sweden; stefan@astro.su.se
[26] The Oskar Klein Centre for Cosmoparticle Physics, AlbaNova, SE-106 91 Stockholm, Sweden
[27] Dipartimento di Fisica, Università di Udine and Istituto Nazionale di Fisica Nucleare, Sezione di Trieste, Gruppo Collegato di Udine, I-33100 Udine, Italy
[28] CNRS/IN2P3, Centre d'Études Nucléaires Bordeaux Gradignan, UMR 5797, Gradignan, 33175, France
[29] Université de Bordeaux, Centre d'Études Nucléaires Bordeaux Gradignan, UMR 5797, Gradignan, 33175, France
[30] Osservatorio Astronomico di Trieste, Istituto Nazionale di Astrofisica, I-34143 Trieste, Italy
[31] Department of Physical Sciences, Hiroshima University, Higashi-Hiroshima, Hiroshima 739-8526, Japan
[32] Center for Space Plasma and Aeronomic Research (CSPAR), University of Alabama in Huntsville, Huntsville, AL 35899, USA
[33] Institució Catalana de Recerca i Estudis Avançats (ICREA), Barcelona, Spain
[34] Department of Physics, Center for Cosmology and Astro-Particle Physics, The Ohio State University, Columbus, OH 43210, USA
[35] Research Institute for Science and Engineering, Waseda University, 3-4-1, Okubo, Shinjuku, Tokyo, 169-8555 Japan
[36] Department of Physics, Tokyo Institute of Technology, Meguro City, Tokyo 152-8551, Japan
[37] Cosmic Radiation Laboratory, Institute of Physical and Chemical Research (RIKEN), Wako, Saitama 351-0198, Japan
[38] Centre d'Étude Spatiale des Rayonnements, CNRS/UPS, BP 44346, F-30128 Toulouse Cedex 4, France
[39] Department of Astronomy, Stockholm University, SE-106 91 Stockholm, Sweden
[40] Physics Department, Università di Roma "La Sapienza," I-00185 Roma, Italy
[41] Department of Physics and Department of Astronomy, University of Maryland, College Park, MD 20742, USA

[42] Istituto Nazionale di Fisica Nucleare, Sezione di Roma "Tor Vergata," I-00133 Roma, Italy
[43] Department of Physics and Astronomy, University of Denver, Denver, CO 80208, USA
[44] Institute of Space and Astronautical Science, JAXA, 3-1-1 Yoshinodai, Sagamihara, Kanagawa 229-8510, Japan
[45] Hiroshima Astrophysical Science Center, Hiroshima University, Higashi-Hiroshima, Hiroshima 739-8526, Japan
[46] Max-Planck Institut für extraterrestrische Physik, 85748 Garching, Germany
[47] Institut für Astro- und Teilchenphysik and Institut für Theoretische Physik, Leopold-Franzens-Universität Innsbruck, A-6020 Innsbruck, Austria
[48] Santa Cruz Institute for Particle Physics, Department of Physics and Department of Astronomy and Astrophysics, University of California at Santa Cruz, Santa Cruz, CA 95064, USA
[49] Department of Physics, Royal Institute of Technology (KTH), AlbaNova, SE-106 91 Stockholm, Sweden
[50] Space Sciences Division, NASA Ames Research Center, Moffett Field, CA 94035-1000, USA
[51] Department of Chemistry and Physics, Purdue University Calumet, Hammond, IN 46323-2094, USA
[52] Consorzio Interuniversitario per la Fisica Spaziale (CIFS), I-10133 Torino, Italy
[53] INTEGRAL Science Data Centre, CH-1290 Versoix, Switzerland
[54] Dipartimento di Fisica, Università di Roma "Tor Vergata," I-00133 Roma, Italy
[55] School of Pure and Applied Natural Sciences, University of Kalmar, SE-391 82 Kalmar, Sweden
Received 2010 April 1; accepted 2010 June 12; published 2010 September 22

ABSTRACT

This paper presents light curves as well as the first systematic characterization of variability of the 106 objects in the high-confidence *Fermi* Large Area Telescope Bright AGN Sample (LBAS). Weekly light curves of this sample, obtained during the first 11 months of the *Fermi* survey (2008 August 4–2009 July 4), are tested for variability and their properties are quantified through autocorrelation function and structure function analysis. For the brightest sources, 3 or 4 day binned light curves are extracted in order to determine power density spectra (PDSs) and to fit the temporal structure of major flares. More than 50% of the sources are found to be variable with high significance, where high states do not exceed 1/4 of the total observation range. Variation amplitudes are larger for flat spectrum radio quasars and low/intermediate synchrotron frequency peaked BL Lac objects. Autocorrelation timescales derived from weekly light curves vary from four to a dozen of weeks. Variable sources of the sample have weekly and 3–4 day bin light curves that can be described by $1/f^{\alpha}$ PDS, and show two kinds of gamma-ray variability: (1) rather constant baseline with sporadic flaring activity characterized by flatter PDS slopes resembling flickering and red noise with occasional intermittence and (2)—measured for a few blazars showing strong activity—complex and structured temporal profiles characterized by long-term memory and steeper PDS slopes, reflecting a random walk underlying mechanism. The average slope of the PDS of the brightest 22 FSRQs and of the 6 brightest BL Lacs is 1.5 and 1.7, respectively. The study of temporal profiles of well-resolved flares observed in the 10 brightest LBAS sources shows that they generally have symmetric profiles and that their total duration vary between 10 and 100 days. Results presented here can assist in source class recognition for unidentified sources and can serve as reference for more detailed analysis of the brightest gamma-ray blazars.

Key words: BL Lacertae objects: general – gamma rays: galaxies – gamma rays: general – methods: data analysis – methods: statistical – quasars: general

Online-only material: color figures, machine-readable table

1. INTRODUCTION

The high energy emission and the erratic, rapid and large-amplitude variability observed in all accessible spectral regimes (radio-to-gamma-ray) are two of the main defining properties of blazars (e.g., Ulrich et al. 1997; Webb 2006). The entire non-thermal continuum is believed to originate mainly in a relativistic jet, pointing close to our line of sight. Studies of variability in different spectral bands and correlations of multi-waveband variability patterns allow us to shed light on the physical processes in action in blazars, such as particle acceleration and emission mechanisms, relativistic beaming, origin of flares and size, structure, and location of the emission regions.

A proper understanding of the physical mechanisms responsible for variability is contingent upon a mathematical and statistical description of the phenomena. The study of variability is particularly important in gamma-ray astronomy. First, it assists in detecting faint sources, discriminating between real point sources and background fluctuations. Second, correlated multi-wavelength variability helps to recognize and identify the correct radio/optical/X-ray source counterparts within the gamma-ray position error box. A characterization of stand-alone gamma-ray variability for unidentified sources can also support the recognition of the correct source class (Nolan et al. 2003).

Even though it has already been studied for many years, the details of blazar variability in various bands have not yet been consistently compared against each other. A major contribution to our current understanding of the blazar phenomenon has been provided by EGRET, which discovered blazars as the largest class of identified and variable gamma-ray sources, in the band above 100 MeV. EGRET blazars showed variations on timescales from days to months (for the sources observed in several viewing periods) and gamma-ray flares on short timescales (1–3 days) have been detected in PKS 0528+134, 3C 279, PKS 1406−076, PKS 1633+382, PKS 1622−297, 3C 454.3 (see, e.g., von Montigny et al. 1995; Wallace et al. 2000; Nolan et al. 2003; Thompson 2006). In some cases, giant γ-ray outbursts were also found by EGRET (as for 3C 279; Hartman et al. 2001), and very rapid variability at very high energy was resolved (for example by HESS in PKS 2155−304; Aharonian et al. 2007). However, a complete characterization of the blazar

[56] Royal Swedish Academy of Sciences Research Fellow, funded by a grant from the K. A. Wallenberg Foundation.
[57] Partially supported by the International Doctorate on Astroparticle Physics (IDAPP) program.
[58] Corresponding and first contact author: stefano.ciprini@pg.infn.it; Co-contact authors: stefan@astro.su.se; Gino.Tosti@pg.infn.it; sarac@slac.stanford.edu.

gamma-ray variability was limited by statistics, number of the observations, and the EGRET pointed operating mode.

A new view on the gamma-ray variable sky is coming from the *Fermi* Large Area Telescope (LAT). Thanks to its large field of view (FOV; covering 20% of the sky at any instant and the full sky in about 3 hr), improved effective area and sensitivity, and the all-sky operating mode, the LAT is, therefore, an unprecedented instrument to monitor the variability emission of blazars in the energy band 20 MeV to >300 GeV (see, e.g., Atwood et al. 2009; Abdo et al. 2009a, 2010a). A major result obtained by the *Fermi* LAT during the first 3 months of observations was the publication of the Bright Source List (BSL; i.e., the 0FGL catalog; Abdo et al. 2009b), a list of 205 sources detected with a significance $>10\sigma$. Of these, 106 sources located at $|b| > 10^\circ$ have been associated with high confidence with known active galactic nuclei (AGNs) and constitute the LAT Bright AGN sample (LBAS). The LBAS sample include two radio galaxies (Cen A and NGC 1275) and 104 blazars of which 58 are flat spectrum radio quasars (FSRQs), 42 are BL Lac objects, and 4 are blazars with uncertain classification (Abdo et al. 2009a).

This paper reports analysis results on the 11 month light curves of these 3 month selected bright AGNs, mostly blazars. Many of the light curves are, in fact, bright in the beginning of the considered 11 month period and then fade. This does not represent a particular bias, as also in the 11 month detected source catalog (Abdo et al. 2010a; first year LAT catalog, 1FGL) on average these sources are among the brightest blazars. A parallel and detailed study of spectral properties on the same LBAS sample is presented in Abdo et al. (2010b) while our analysis provides a temporal and flux variability analyses on the same sample. In Abdo et al. (2010b), the weekly gamma-ray spectral photon index is measured, in general, to vary in time only modestly (by <0.2–0.3) despite large variability of flux, and to vary only modestly within different blazar subclasses. In our paper, significant gamma-ray flux variability for about half of the LBAS objects is reported and for 1/4 of the sources, significant flares and outbursts are also found, showing a much stronger and violent variability of the flux than of the photon index.

In the following, we use a ΛCDM (concordance) cosmology with values given within 1σ of the *Wilkinson Microwave Anisotropy Probe* results (Komatsu et al. 2009), namely, Hubble constant value $H_0 = 71\,\mathrm{km\,s^{-1}\,Mpc^{-1}}, \Omega_m = 0.27, \Omega_\Lambda = 0.73$.

In Section 2, a description of the LAT observation and light curve extraction is reported, while in Section 3, results of variability search and amplitude quantification are presented. In Section 4, global variability properties of weekly bin light curves are presented through autocorrelation and structure function (SF) analysis. The analysis of the power spectral density and flare temporal profiles is presented in Sections 5 and 6, respectively, using finer sampling (3 and 4 day bins) light curves for the brightest sources. Summary and conclusions are given in Section 7. Cross-correlation studies between the γ-ray and other bands (such as radio-mm and optical bands), as well as more detailed studies on periodicity search, will be covered by other works based on the brightest sources where it is possible to obtain a finer-sampled flux light curves.

2. OBSERVATIONS WITH THE LAT AND LBAS LIGHT CURVES

The *Fermi* LAT (Atwood et al. 2009; Abdo et al. 2009d) is a pair-conversion gamma-ray telescope sensitive to photon energies greater than 20 MeV. It consists of a tracker (composed of two sections, front and back, with different capabilities), a calorimeter, and an anticoincidence system to reject the charged-particle background. The LAT has a large peak effective area (~8000 $\mathrm{cm^2}$ for 1 GeV photons in the event class considered here), viewing ≃2.4 sr of the full sky with angular resolution (68% containment radius) better than $\simeq 1^\circ$ at $E = 1$ GeV.

Data used in this paper were collected during the first 11 months of the nominal all-sky survey, from 2008 August 4 to 2009 July 4 (Modified Julian Day (MJD) from 54682.655 to 55016.620).

In order to avoid background contamination from the bright Earth limb, time intervals where the Earth entered the LAT FOV were excluded from this study (corresponding to a rocking angle larger than 47°). In addition, events that were reconstructed within 8° of the Earth limb were excluded from the analysis (corresponding to a zenith angle cut of 105°). Due to uncertainties in the current calibration and the necessity of a trade-off between error accuracy and event statistics, only photons belonging to the "Diffuse" class and with energies above 100 MeV were retained. This event analysis was performed with the standard *Fermi* LAT `ScienceTools` software package[59] (version v9r12) using in particular the tool `gtlike`, and using the first set of instrument response functions (IRFs) tuned with the flight data (P6_V3_DIFFUSE). In contrast to the preflight version, these IRFs take into account corrections for pile-up events. Since this is higher for lower energy photons, the measured photon index of a given source is about 0.1 higher (i.e., the spectrum is softer) with this IRF set as compared to the P6_V1_DIFFUSE one used previously in Abdo et al. (2009a, 2009b).

The light curves of all the LBAS sources were built using 7 day time intervals, for a total of 47 bins. For the brightest sources light curves were built using also time bins of 3 and 4 days (see Section 6). For each time bin, the flux, photon index, and test statistic (TS) of each source were determined, using the maximum-likelihood algorithm implemented in `gtlike`. The TS is defined as TS = 2Δlog(likelihood) between models with and without the source and it is a measure of the source significance (Mattox et al. 1996).

Photons were selected in a region of interest (RoI) 7° in radius centered on the position of the source of interest. In the RoI analysis, the sources were modeled as simple power law ($F = dN/dE = N_0 E^{-p}$). The isotropic background (the sum of residual instrumental background and extragalactic diffuse gamma-ray background) was modeled with a simple power law. The GALPROP model version `gll_iem_v01.fit` (Strong et al. 2004a, 2004b) was used for the Galactic diffuse emission, with both flux and spectral photon index left free in the model fit. All errors reported in the figures or quoted in the text are 1σ statistical errors. The estimated systematic uncertainty on the flux is 10% at 100 MeV, 5% at 500 MeV, and 20% at 10 GeV.

For the 106 weekly light curves of LBAS sources analyzed in Sections 3 and 4, the flux in each time bin is reported for the energy band $E > 300$ MeV. This is the best band for reporting the flux because it is the band for which we have the highest signal to noise ratio for each source. The 3 day and 4 day bin light curves of the brightest sources analyzed in Sections 5 and 6 are extracted using the F($E > 100$ MeV) flux.

[59] http://fermi.gsfc.nasa.gov/ssc/data/analysis/documentation/Cicerone/

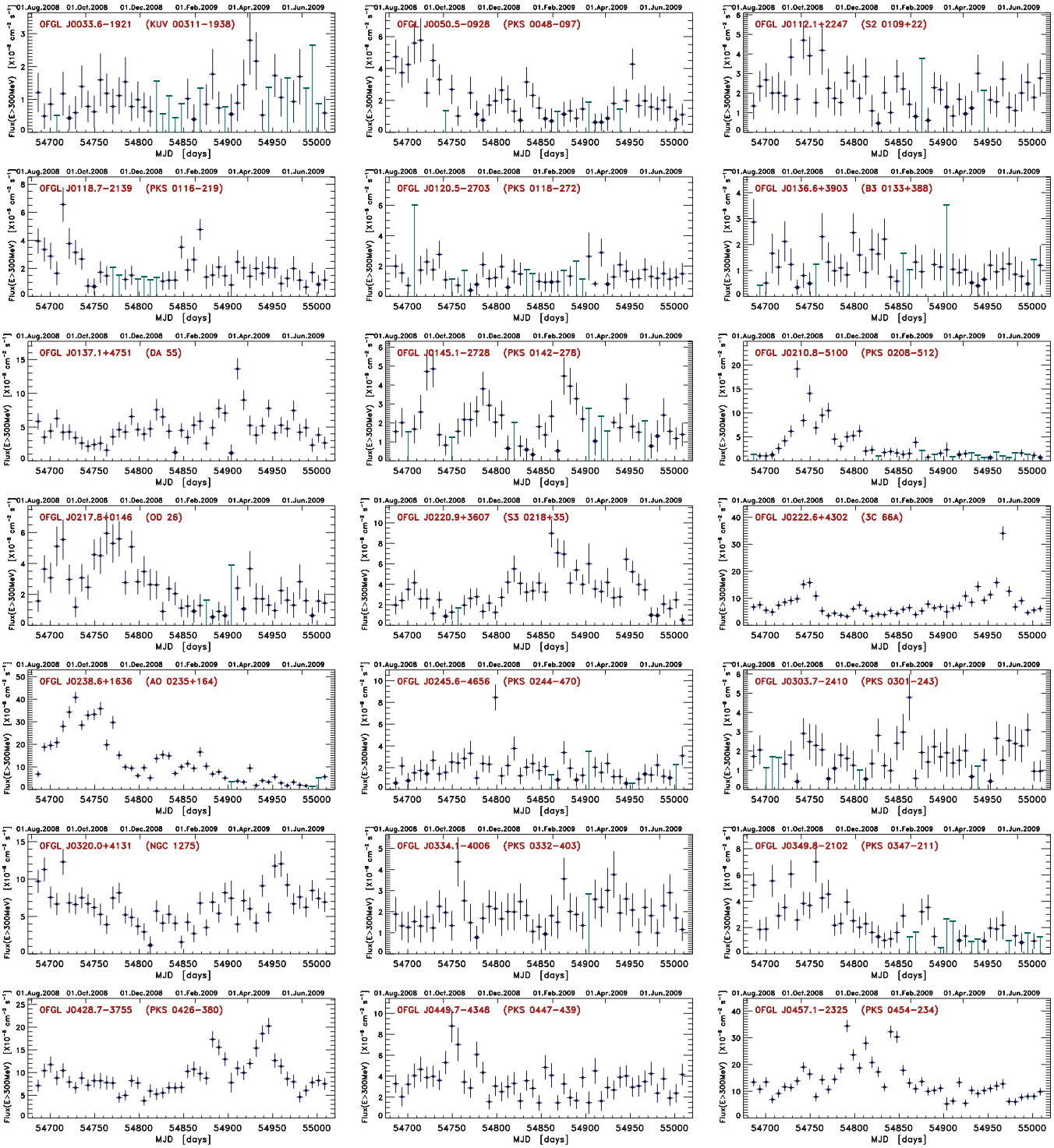

Figure 1. Light curves of the integrated flux ($E > 300$ MeV) measured in and averaged on weekly time bins obtained with the standard tool `gtlike`. In this figure, all the 84 LBAS objects that are selected for temporal variability study are reported. Filled circle symbols represent the best-fit values of the flux in the weekly bin with TS $\geqslant 4$ (approximatively 2σ), open circle symbols are the best-fit values of the flux in the bin with $1 <$ TS < 4, and the bars are the values of 1σ upper limits in the bin. Data in these plots are also available in Table 3 in the Appendix.

(A color version of this figure is available in the online journal.)

3. VARIABILITY SEARCH AND AMPLITUDE IN WEEKLY LIGHT CURVES

The following variability analysis was performed using the weekly light curves reported in Figures 1 and 2. We used $F(E > 300$ MeV) (hereafter F_{300}) in order to enable the comparison of the observed variability characteristics for the different sources.

Because of the intrinsically variable nature of blazars for several sources we were not able to obtain a highly significant (TS $\geqslant 25$) estimate of the flux for all the 47 weeks. Therefore, in building the light curves we followed the same approach

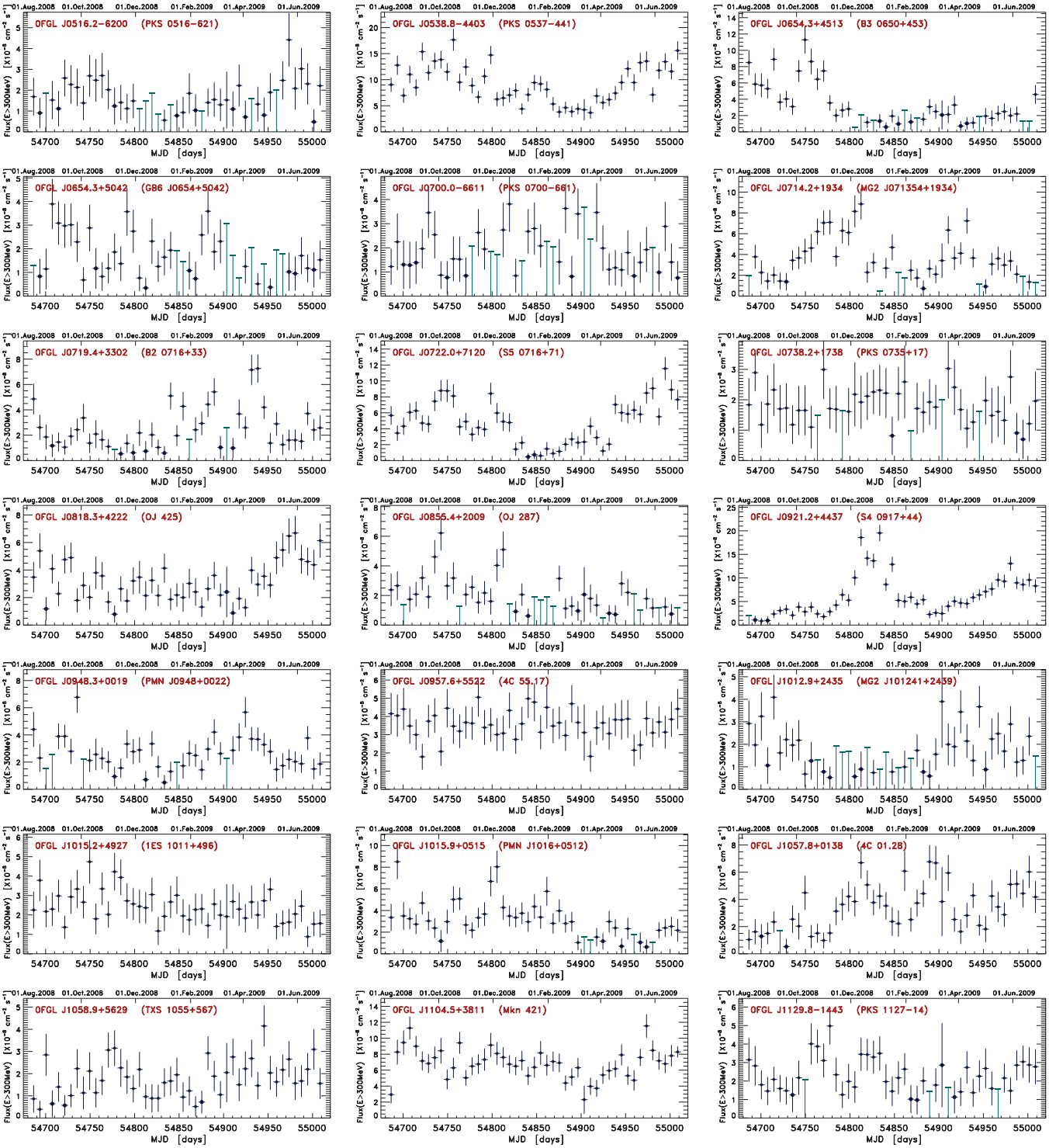

Figure 1. (Continued)

described in Abdo et al. (2009b) to preserve the maximum number of data points. For each time bin, we keep the best-fit value of the flux and its estimated error even when the source is below 5σ significance. Whenever TS $\leqslant 1$ we computed the 1σ upper limit and replaced the best-fit value of the flux with that upper limit. The weekly bin light curves extracted are presented in Figures 1 and 2, where filled circle symbols represent the best-fit values of the integrated flux ($E > 300$ MeV) in the weekly bin with TS $\geqslant 4$ (approximatively $>2\sigma$), open circle symbols are the best-fit values of the flux in the bin having $1 <$ TS < 4, and the bars are the values of 1σ upper limits in the bin.

We investigated whether a source had significant variations using a simple χ^2 test,

$$\chi^2 = \sum_{i=1}^{N_p} \frac{(F_i - \langle F_i \rangle^2)}{(\sigma_i^2 + \sigma_{\rm syst}^2)}, \quad (1)$$

where F_i are the F_{300} fluxes of each source on each bin and σ_i

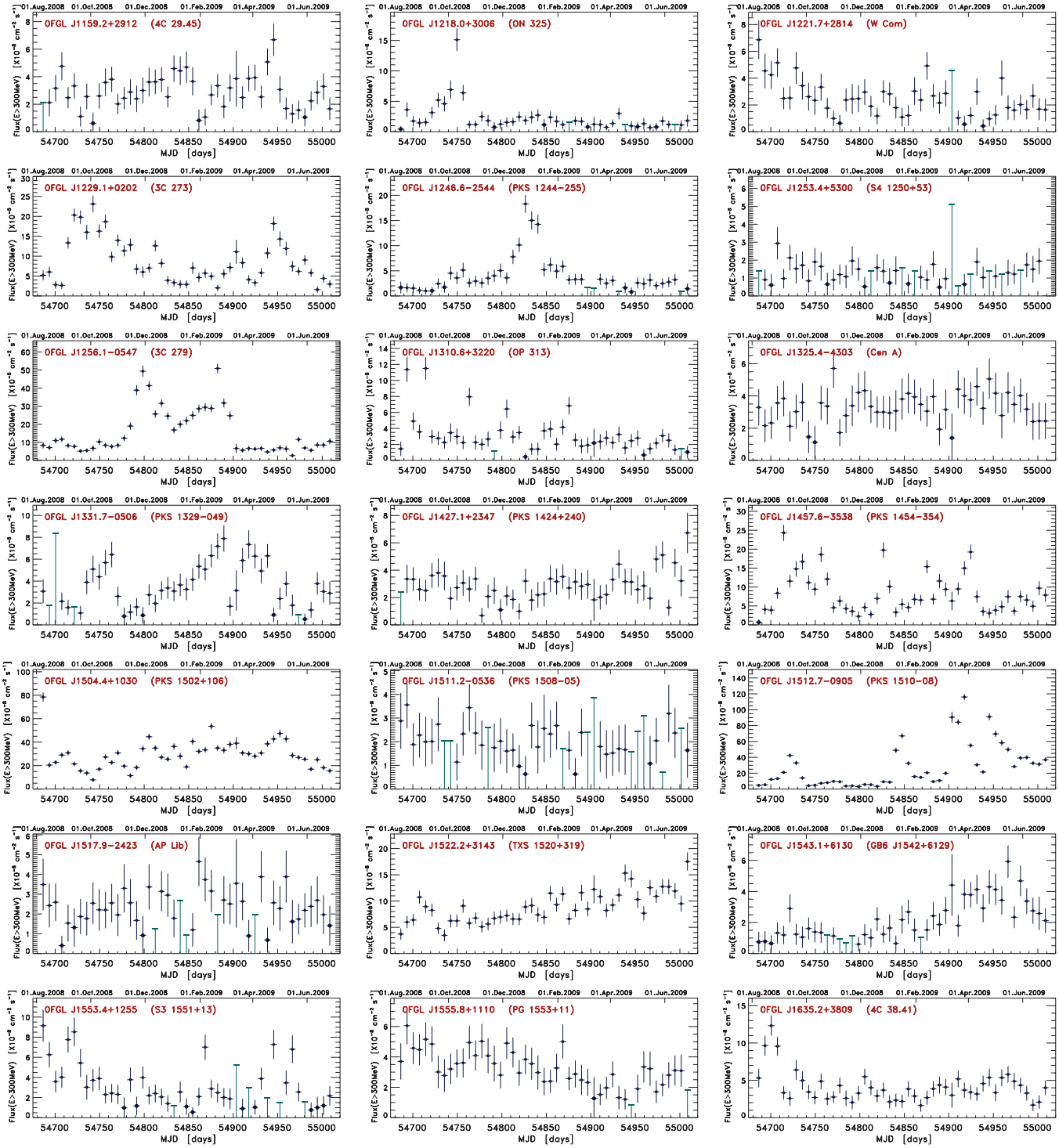

Figure 1. (Continued)

is the statistical uncertainty to which we added in quadrature $\sigma_{\rm syst} = 0.03\langle F_i\rangle$ as an estimate of the systematic error (Abdo et al. 2009a, 2009d); N_p is the number of points in each light curve having a TS $\geqslant 4(\sim 2\sigma)$; and $\langle F_i\rangle$ is the unweighted mean of the flux. This test was applied to light curves containing only flux values with TS $\geqslant 4$ and excluding upper limits and fluxes with $\sigma_i/F_i > 0.5$ (see Figure 3). Figure 4 shows the distribution of the "coverage" fraction $N_p/N_{\rm tot}$, that is, the detection fraction of the total period of observation after this cut on the TS. The weekly light curves for the 84 LBAS objects for which this fraction is >60%, i.e., having at least 28 detections with TS $\geqslant 4$, are shown in Figure 1. The light curves of lower quality corresponding to the remaining 22 sources are shown in Figure 2.

We also quantify the variability amplitude of all the LBAS sources, using the "normalized excess variance" (Nandra et al. 1997; Edelson et al. 2002). This estimator is defined by

$$\sigma^2_{\rm NXS} = \frac{S^2 - \langle\sigma^2_{\rm err}\rangle}{\langle F_i\rangle^2}, \qquad (2)$$

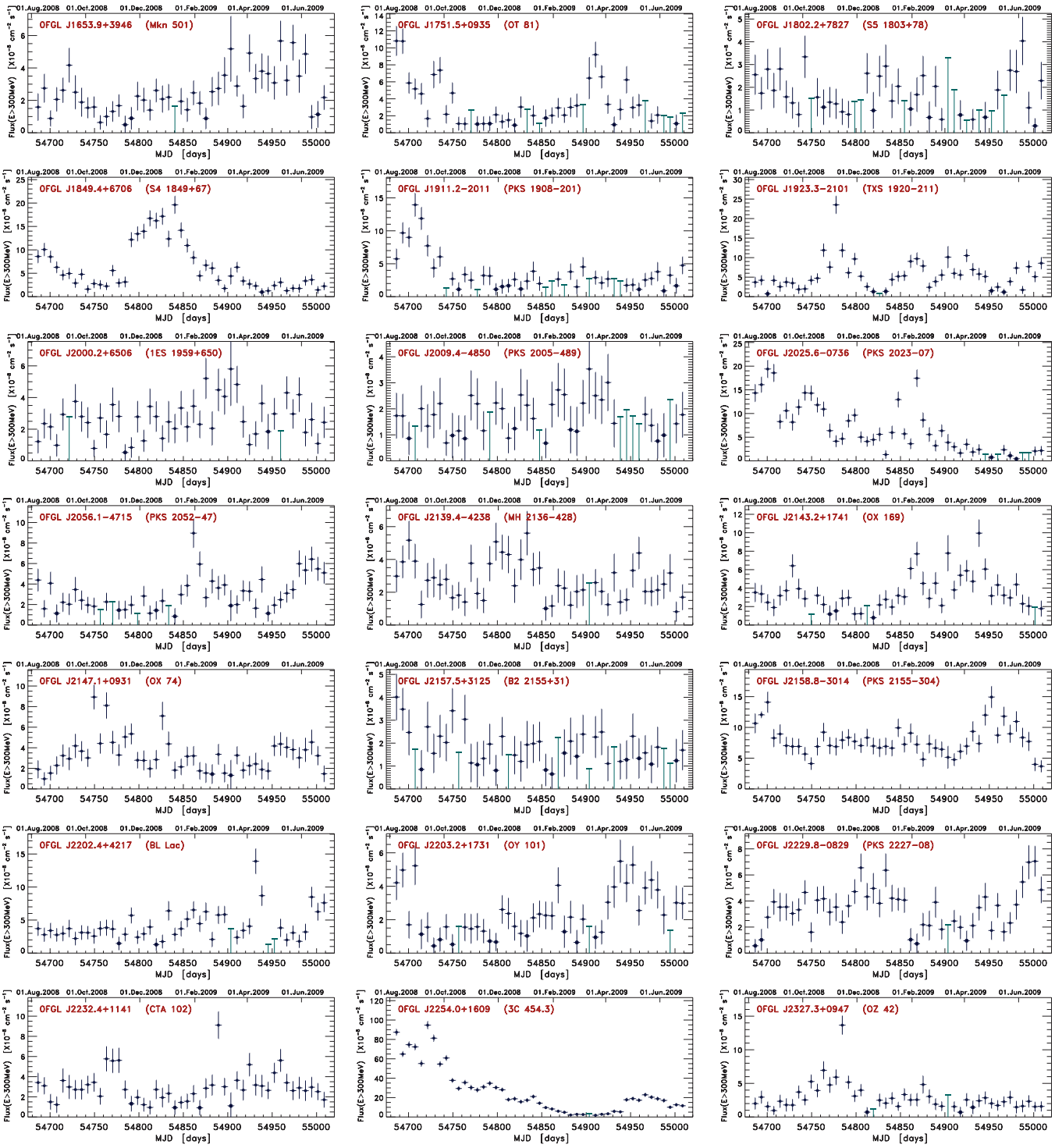

Figure 1. (Continued)

where S^2 is the variance of the light curve and $\sigma^2_{\rm err} = \sigma_i^2 + \sigma^2_{\rm sys}$. The error in $\sigma^2_{\rm NXS}$ was evaluated according to the prescription of Vaughan et al. (2003).

The results of this analysis are reported in Table 1: the first column lists the bright source list (0FGL list) name, Column 2 the other source name, and Column 3 the optical class. In the fourth column, we report the spectral energy distribution (SED) class, based on the peak frequency of the synchrotron component ($\nu_{\rm p}^{\rm S}$) of the broadband SED following the scheme outlined by Abdo et al. (2010c) which is an extension of the classification system introduced by Padovani & Giommi (1995) for BL Lacs. In this scheme we have: low synchrotron peaked (LSP; for $\nu^{\rm S}_{\rm peak} < 10^{14}$ Hz), intermediate synchrotron peaked (ISP; for 10^{14} Hz $< \nu^{\rm S}_{\rm peak} < 10^{15}$ Hz), and high synchrotron peaked (HSP; for $\nu^{\rm S}_{\rm peak} > 10^{15}$ Hz) blazars. Data listed in Columns 5–13 are the redshift, N_p, the mean flux, the standard deviation of each light curve, the peak flux and error, the variability probability of χ^2 (for $N_p - 1$ degrees of freedom), and the normalized excess variance and error. Negative values of $\sigma^2_{\rm NXS}$ indicate absence or very small variability and/or slightly overestimated errors.

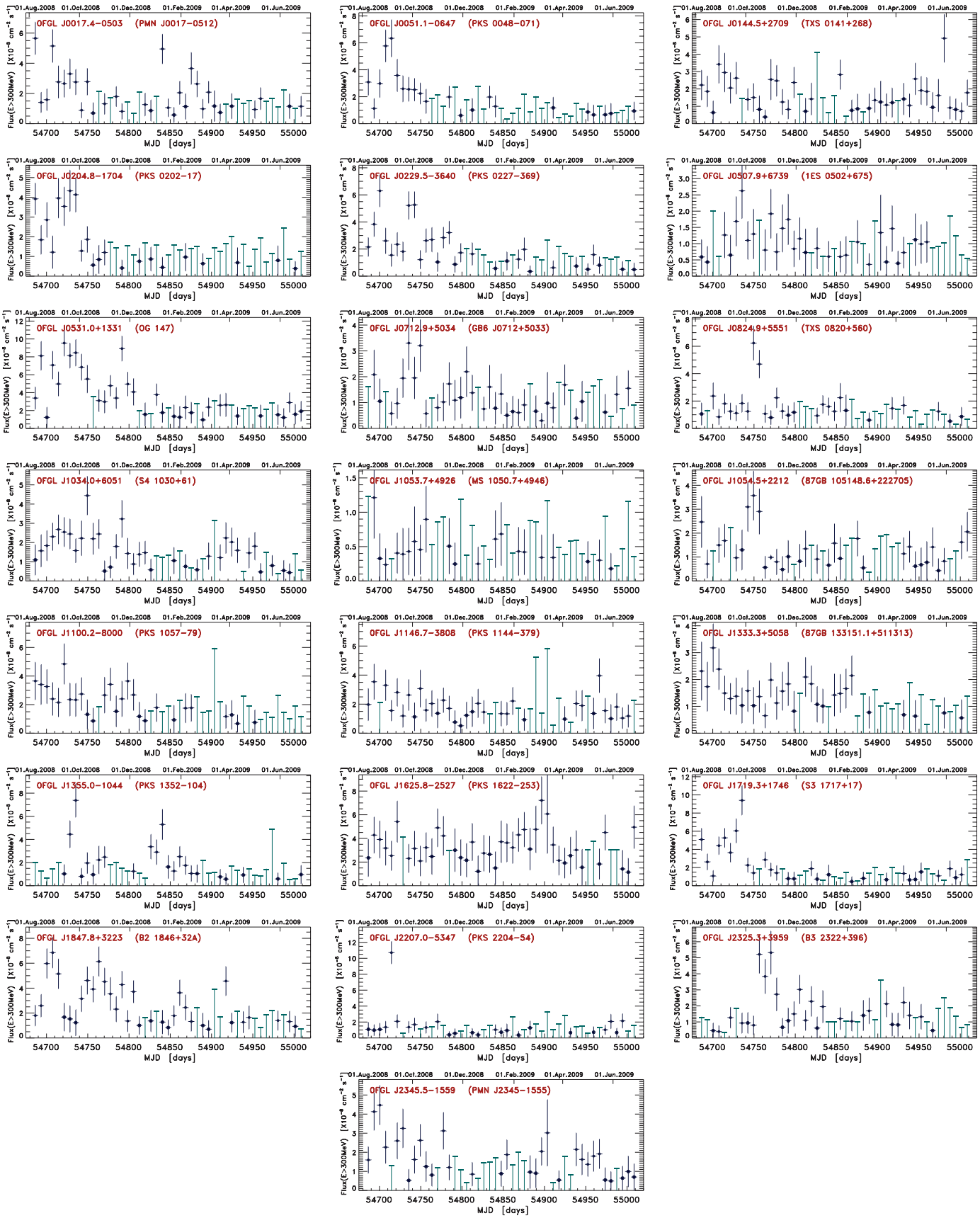

Figure 2. Twenty-two light curves that are excluded by the temporal analysis adopting the constraint of at least 60% of bins having a TS $\geqslant 4$ detection. Among these we note three peculiar light curves for the LSP blazars 0FGL J0531.0+1331, 0FGL J1719.3+1746, and 0FGL J2207.0−5347, showing strong flares and flux activity but only during a limited portion of the 11 months observed. Data appearing these plots are available in Table 3 in the Appendix.

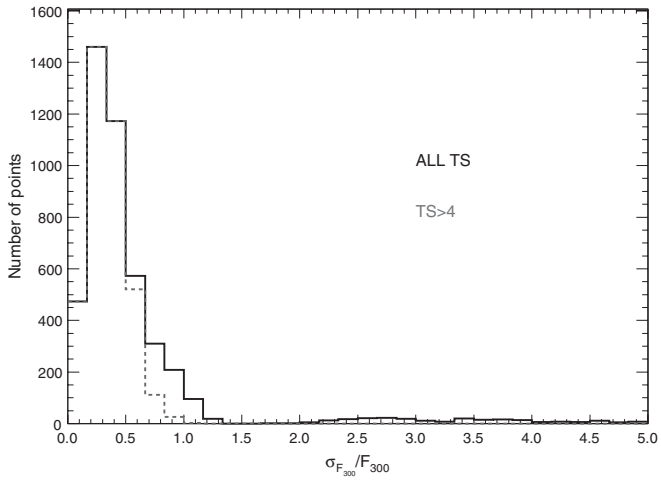

Figure 3. Distribution of the relative flux errors $\sigma_{F_{300}}/F_{300}$ for all the 106 LBAS light curves and all the data points. The larger values of the relative error in the distribution labeled "All TS" are due to the counting of upper limits.

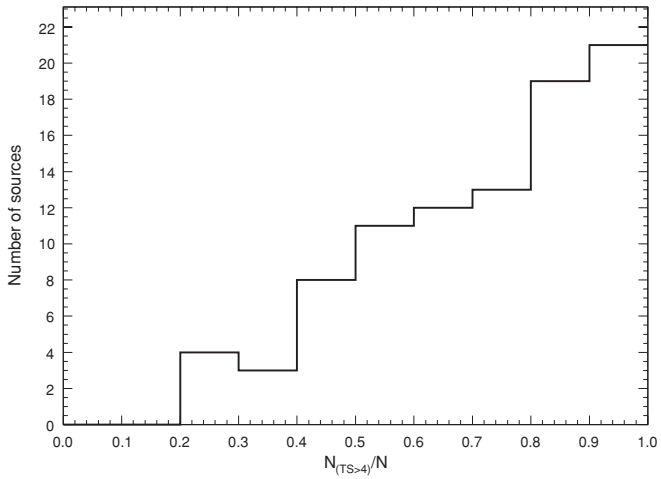

Figure 4. Distribution of the coverage fraction N_p/N of the observation period of each light curve.

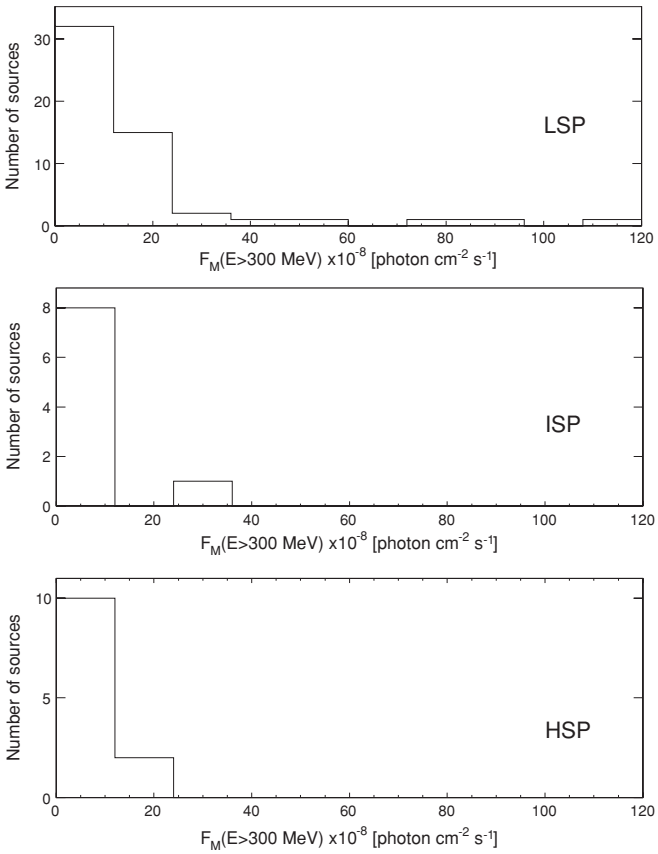

Figure 5. Distribution of F_M for the LSP, ISP, and HSP light curves with a coverage factor $N_p/N \geqslant 60\%$.

The large majority of sources (74) belong to the LSP class, which includes all FSRQs (58) and several BL Lacs (16), while both ISP and HSP classes have each 13 BL Lacs sources. There are also two radio galaxies (NGC 1275 also known as Per A and Cen A) and four objects which cannot be well classified for paucity of data.

On the basis of the χ^2 test, variability was detected in 68 out of the 106 LBAS sources with a significance higher than 99% (Column 11 in Table 1). Note, however, that as demonstrated by Figure 19 in Abdo et al. (2010e) the χ^2 has a strong dependence on the statistical flux uncertainties. For the fainter sources this leads to a reduction of the χ^2 for a given fractional flux variation and then a source can be considered significantly variable only if it is both intrinsically variable and sufficiently bright. Therefore, fainter sources can appear less variable than brighter sources simply because we cannot measure their variability.

In Abdo et al. (2009a), 56 sources were flagged as variable based on the results of a χ^2 test applied to weekly light curves covering the first 3 months of operation. To compare our results with those reported in Abdo et al. (2009a), we divided the light curves in four consecutive segments having a duration of about 12 weeks, and the χ^2 test was applied to each of them. Forty two sources were found variable with a significance higher than 99% during the first light curve segment (corresponding to about the same time interval analyzed in Abdo et al. 2009a, 2009b; 28 in the second, 23 in the third, and 19 in the last). The difference in the number of variable sources in the first segment with respect to Abdo et al. (2009a) results can be explained by taking into account that in Abdo et al. (2009a) all light curve data points, including those with TS < 4, were considered in the calculation of the χ^2 and the likelihood analysis was performed with a different combination of IRFs and diffuse models. The decreasing number of variable sources revealed in the four time intervals is a selection effect. We are using the BSL sample, so there are disproportionately more objects which happened to flare up at the beginning of the interval and then faded. However, this is illustrative of one of the distinctive aspects of the intrinsic characteristics of the blazars' variability: alternate periods of flaring and low activity states. However, the total period of our observations is in most cases still too short to allow an estimation of the duty cycle of the blazar variability in the gamma-ray energy range. Flux distributions can be used to characterize the gamma-ray duty cycle, and for two FSRQs (3C 454.3 and PKS 1510−08) that were very active during the first 1.5 years of LAT observations, the fluxes are found distributed in a different way with respect to a lognormal distribution (Tavecchio et al. 2010).

Figure 5 shows the distribution of the peak (F_M) values for LSP, ISP, and HSP. It can be noted that only a few LSP were detected in exceptionally bright states with a flux $F_M > 2 \times 10^{-7}$ photon cm^{-2} s^{-1}.

Figures 6 and 7 show the distributions of $\sigma^2_{\rm NXS}$ and of the ratio between the highest measured flux to the mean $F_M/\langle F \rangle$ for the

Table 1
Variability Indices and Amplitudes

0FGL	Other Name	Optical Class	SED Class	z	N_p	$\langle F_{300}\rangle$[a]	S[a]	F_M[a]	σ_M[a]	Prob	$\sigma^2_{\rm NXS}$	err$\left(\sigma^2_{\rm NXS}\right)$
J0017.4−0503	PMN J0017−0512	FSRQ	LSP	0.227	24	2.30	1.37	5.65	1.07	> 99.0	0.24	0.08
J0033.6−1921	KUV 00311−1938	BLLac	HSP	0.610	31	1.12	0.52	2.80	1.04	12.0	−0.09	0.08
J0050.5−0928	PKS 0048−097	BLLac	ISP	>0.30	32	2.51	1.32	5.77	1.37	>99.0	0.16	0.06
J0051.1−0647	PKS 0048−071	FSRQ	LSP	1.975	14	2.84	1.47	6.34	1.38	>99.0	0.17	0.09
J0112.1+2247	S2 0109+22	BLLac	ISP	>0.23	39	2.20	0.88	4.70	0.97	69.8	0.02	0.04
J0118.7−2139	PKS 0116−219	FSRQ	LSP	1.165	39	2.07	1.19	6.56	1.21	>99.0	0.19	0.06
J0120.5−2703	PKS 0118−272	BLLac	LSP	0.557	34	1.52	0.55	2.89	0.91	1.8	−0.11	0.06
J0136.6+3903	B3 0133+388	BLLac	HSP	...	34	1.29	0.55	2.87	0.89	11.8	−0.07	0.06
J0137.1+4751	DA 55	FSRQ	LSP	0.859	45	4.89	2.13	13.62	1.56	>99.0	0.13	0.03
J0144.5+2709	TXS 0141+268	BLLac	ISP	...	26	1.98	0.91	4.92	1.38	72.3	0.03	0.06
J0145.1−2728	PKS 0142−278	FSRQ	LSP	1.148	33	2.32	1.05	4.85	0.96	>99.0	0.10	0.05
J0204.8−1704	PKS 0202−17	FSRQ	LSP	1.740	11	2.74	1.22	4.33	1.05	>99.0	0.12	0.08
J0210.8−5100	PKS 0208−512	FSRQ	LSP	1.003	30	4.43	4.22	19.19	1.79	>99.0	0.87	0.09
J0217.8+0146	OD 26	FSRQ	LSP	1.715	40	2.70	1.47	5.95	1.36	>99.0	0.19	0.05
J0220.9+3607	S3 0218+35	FSRQ	LSP	0.944	42	3.55	1.71	8.98	1.37	>99.0	0.15	0.04
J0222.6+4302	3C 66A	BLLac	ISP	0.444	47	7.92	5.05	34.06	2.52	>99.0	0.38	0.03
J0229.5−3640	PKS 0227−369	FSRQ	LSP	2.115	20	2.62	1.45	6.30	1.18	>99.0	0.22	0.07
J0238.6+1636	AO 0235+164	BLLac	LSP	0.940	44	13.19	10.73	40.78	2.42	>99.0	0.66	0.03
J0245.6−4656	PKS 0244−470	Un	...	...	35	2.20	1.28	8.46	1.18	>99.0	0.20	0.07
J0303.7−2410	PKS 0301−243	BLLac	HSP	0.260	36	1.95	0.78	4.78	1.19	43.3	−0.01	0.04
J0320.0+4131	NGC 1275	RG	...	0.018	46	6.54	2.42	12.30	1.71	>99.0	0.09	0.02
J0334.1−4006	PKS 0332−403	BLLac	LSP	...	44	1.98	0.72	4.36	1.16	15.1	−0.04	0.04
J0349.8−2102	PKS 0347−211	FSRQ	LSP	2.944	33	2.86	1.51	7.00	1.55	>99.0	0.18	0.05
J0428.7−3755	PKS 0426−380	BLLac	LSP	1.112	47	9.19	3.58	20.24	1.74	>99.0	0.13	0.02
J0449.7−4348	PKS 0447−439	BLLac	HSP	0.205	47	3.40	1.44	8.79	1.55	>99.0	0.09	0.03
J0457.1−2325	PKS 0454−234	FSRQ	LSP	1.003	47	13.56	6.78	34.39	2.23	>99.0	0.24	0.02
J0507.9+6739	1ES 0502+675	BLLac	HSP	0.416	23	1.14	0.50	2.63	0.85	6.3	−0.14	0.10
J0516.2−6200	PKS 0516−621	Un	...	...	29	1.95	0.74	4.42	1.28	9.1	−0.08	0.06
J0531.0+1331	PKS 0528+134	FSRQ	LSP	2.070	22	5.04	2.34	9.54	1.46	>99.0	0.15	0.05
J0538.8−4403	PKS 0537−441	BLLac	LSP	0.892	47	9.23	3.58	17.65	2.06	>99.0	0.13	0.02
J0654.3+4513	B3 0650+453	FSRQ	LSP	0.933	32	4.10	2.63	11.29	1.66	>99.0	0.35	0.06
J0654.3+5042	GB6 J0654+5042	Un	...	...	28	2.00	0.94	3.89	1.06	91.4	0.06	0.06
J0700.0−6611	PKS 0700−661	Un	...	...	29	2.12	0.87	3.81	1.15	39.4	−0.02	0.05
J0712.9+5034	GB6 J0712+5033	BLLac	ISP	...	24	1.40	0.76	3.30	1.04	69.3	0.03	0.09
J0714.2+1934	MG2 J071354+1934	FSRQ	LSP	0.534	37	3.98	1.97	8.85	1.48	>99.0	0.17	0.04
J0719.4+3302	B2 0716+33	FSRQ	LSP	0.779	37	2.78	1.59	7.26	1.11	>99.0	0.23	0.06
J0722.0+7120	S5 0716+71	BLLac	ISP	0.310	45	4.94	2.63	11.56	1.44	>99.0	0.24	0.03
J0738.2+1738	PKS 0735+17	BLLac	LSP	0.424	39	1.89	0.51	3.03	0.98	0.0	−0.11	0.04
J0818.3+4222	OJ 425	BLLac	LSP	0.530	43	3.36	1.40	6.69	1.23	>99.0	0.09	0.03
J0824.9+5551	TXS 0820+560	FSRQ	LSP	1.417	20	1.91	1.28	6.23	1.25	>99.0	0.32	0.11
J0855.4+2009	OJ 287	BLLac	LSP	0.306	28	2.48	1.22	6.22	1.17	>99.0	0.12	0.06
J0921.2+4437	S4 0917+44	FSRQ	LSP	2.190	44	6.56	4.32	19.52	1.70	>99.0	0.41	0.04
J0948.3+0019	PMN J0948+0022	FSRQ	LSP	0.585	39	2.83	1.16	6.77	1.13	>99.0	0.07	0.04
J0957.6+5522	4C 55.17	FSRQ	LSP	0.896	47	3.55	0.76	5.05	1.07	2.1	−0.03	0.02
J1012.9+2435	MG2 J101241+2439	FSRQ	LSP	1.805	28	2.11	0.93	4.09	0.98	71.7	0.02	0.05
J1015.2+4927	1ES 1011+496	BLLac	HSP	0.212	47	2.40	0.79	4.74	1.12	36.4	−0.01	0.03
J1015.9+0515	PMN J1016+0512	FSRQ	LSP	1.713	38	3.54	1.57	8.50	1.58	>99.0	0.12	0.04
J1034.0+6051	S4 1030+61	FSRQ	LSP	1.401	24	2.00	0.74	4.44	1.01	52.4	0.00	0.04
J1053.7+4926	MS 1050.7+4946	BLLac	ISP	0.140	16	0.50	0.25	1.21	0.59	3.3	−0.33	0.21
J1054.5+2212	87GB 105148.6+222705	BLLac	ISP	...	20	1.64	0.79	3.57	1.03	71.2	0.03	0.08
J1057.8+0138	4C 01.28	FSRQ	LSP	0.888	44	3.50	1.62	6.77	1.21	>99.0	0.12	0.04
J1058.9+5629	TXS 1055+567	BLLac	ISP	0.143	44	1.83	0.79	4.15	0.92	78.7	0.03	0.04
J1100.2−8000	PKS 1057−79	BLLac	LSP	0.569	18	2.69	0.86	4.84	1.42	9.2	−0.08	0.06
J1104.5+3811	Mkn 421	BLLac	HSP	0.030	47	6.84	1.88	11.54	1.46	>99.0	0.04	0.01
J1129.8−1443	PKS 1127−14	FSRQ	LSP	1.184	38	2.44	0.86	4.98	0.99	50.3	0.00	0.03
J1146.7−3808	PKS 1144−379	FSRQ	LSP	1.048	24	2.06	0.77	3.96	1.17	14.4	−0.06	0.06
J1159.2+2912	4C 29.45	FSRQ	LSP	0.729	43	3.06	1.14	6.68	1.17	98.1	0.05	0.03
J1218.0+3006	ON 325	BLLac	HSP	0.130	38	2.51	2.51	15.11	1.82	>99.0	0.90	0.12
J1221.7+2814	W Com	BLLac	ISP	0.102	43	2.58	1.27	6.86	1.44	>99.0	0.12	0.05
J1229.1+0202	3C 273	FSRQ	LSP	0.158	47	8.68	5.47	23.11	2.07	>99.0	0.38	0.03
J1246.6−2544	PKS 1244−255	FSRQ	LSP	0.635	37	4.60	3.81	18.28	1.75	>99.0	0.64	0.07
J1253.4+5300	S4 1250+53	BLLac	LSP	...	29	1.45	0.47	2.93	0.89	0.9	−0.12	0.06
J1256.1−0548	3C 279	FSRQ	LSP	0.536	47	15.69	12.31	50.91	2.61	>99.0	0.62	0.03
J1310.6+3220	OP 313	FSRQ	LSP	0.997	41	3.38	2.31	11.50	1.39	>99.0	0.40	0.06
J1325.4−4303	Cen A	RG	...	0.002	44	3.41	0.82	5.71	1.20	0.8	−0.05	0.02
J1331.7−0506	PKS 1329−049	FSRQ	LSP	2.150	39	3.86	1.86	7.88	1.20	>99.0	0.16	0.04

Table 1
(Continued)

0FGL	Other Name	Optical Class	SED Class	z	N_p	$\langle F_{300}\rangle^{a}$	S^{a}	$F_M{}^{a}$	$\sigma_M{}^{a}$	Prob	$\sigma^2_{\rm NXS}$	err$\left(\sigma^2_{\rm NXS}\right)$
J1333.3+5058	87GB 133151.1+511313	FSRQ	LSP	1.362	20	1.72	0.53	3.18	0.89	4.8	−0.09	0.06
J1355.0−1044	PKS 1352−104	FSRQ	LSP	0.330	13	2.92	1.76	7.38	1.45	>99.0	0.27	0.11
J1427.1+2347	PKS 1424+240	BLLac	ISP	...	45	2.91	1.08	6.73	1.47	94.0	0.04	0.03
J1457.6−3538	PKS 1454−354	FSRQ	LSP	1.424	46	8.49	5.16	24.30	2.08	>99.0	0.34	0.03
J1504.4+1030	PKS 1502+106	FSRQ	LSP	1.839	47	29.57	12.15	78.44	3.79	>99.0	0.17	0.01
J1511.2−0536	PKS 1508−05	FSRQ	LSP	1.185	31	2.17	0.58	3.56	0.99	0.0	−0.14	0.05
J1512.7−0905	PKS 1510−08	FSRQ	LSP	0.360	47	28.67	27.21	115.94	3.82	>99.0	0.91	0.02
J1517.9−2423	AP Lib	BLLac	LSP	0.048	35	2.62	0.76	4.65	1.24	0.5	−0.09	0.04
J1522.2+3143	TXS 1520+319	FSRQ	LSP	1.487	47	8.88	3.01	17.53	1.69	>99.0	0.09	0.01
J1543.1+6130	GB6 J1542+6129	BLLac	ISP	...	39	2.39	1.26	5.93	1.03	>99.0	0.16	0.05
J1553.4+1255	S3 1551+13	FSRQ	LSP	1.308	32	3.92	2.13	9.14	1.57	>99.0	0.22	0.05
J1555.8+1110	PG 1553+11	BLLac	HSP	>0.09	44	3.31	1.12	6.05	1.21	93.2	0.03	0.02
J1625.8−2527	PKS 1622−253	FSRQ	LSP	0.786	26	3.90	1.20	7.21	2.00	3.3	−0.08	0.05
J1635.2+3809	4C 38.41	FSRQ	LSP	1.814	47	4.09	2.06	12.32	1.34	>99.0	0.19	0.04
J1653.9+3946	Mkn 501	BLLac	HSP	0.033	42	2.61	1.27	5.67	1.23	>99.0	0.12	0.05
J1719.3+1746	S3 1717+17	BLLac	LSP	0.137	18	3.04	2.18	9.40	1.61	>99.0	0.44	0.11
J1751.5+0935	OT 81	BLLac	LSP	0.322	33	3.96	2.72	10.82	1.73	>99.0	0.38	0.07
J1802.2+7827	S5 1803+78	BLLac	LSP	0.680	30	1.94	0.85	4.04	1.05	77.3	0.03	0.05
J1847.8+3223	B2 1846+32A	FSRQ	LSP	0.798	24	3.30	1.67	6.85	1.23	>99.0	0.17	0.06
J1849.4+6706	S4 1849+67	FSRQ	LSP	0.657	46	6.31	4.99	19.62	1.86	>99.0	0.60	0.05
J1911.2−2011	PKS 1908−201	FSRQ	LSP	1.119	31	4.35	3.01	13.95	1.77	>99.0	0.40	0.07
J1923.3−2101	TXS 1920−211	FSRQ	LSP	0.874	41	6.18	3.86	23.52	2.25	>99.0	0.34	0.04
J2000.2+6506	1ES 1959+650	BLLac	HSP	0.047	43	2.70	1.19	5.80	2.32	94.8	0.05	0.04
J2009.4−4850	PKS 2005−489	BLLac	HSP	0.071	30	1.96	0.62	3.53	1.71	1.0	−0.11	0.05
J2025.6−0736	PKS 2023−07	FSRQ	LSP	1.388	40	7.60	5.07	19.39	1.85	>99.0	0.42	0.04
J2056.1−4715	PKS 2052−47	FSRQ	LSP	1.491	37	3.41	1.66	8.96	1.41	>99.0	0.15	0.04
J2139.4−4238	MH 2136−428	BLLac	ISP	>0.24	45	2.71	1.18	5.60	1.34	98.4	0.06	0.04
J2143.2+1741	OX 169	FSRQ	LSP	0.213	41	3.75	1.87	9.95	1.47	>99.0	0.17	0.04
J2147.1+0931	OX 74	FSRQ	LSP	1.113	45	3.32	1.66	8.93	1.18	>99.0	0.17	0.04
J2157.5+3125	B2 2155+31	FSRQ	LSP	1.486	28	2.12	0.72	4.01	1.01	8.4	−0.06	0.05
J2158.8−3014	PKS 2155−304	BLLac	HSP	0.116	47	7.89	2.38	14.93	1.75	>99.0	0.06	0.01
J2202.4+4217	BL Lac	BLLac	LSP	0.069	42	4.26	2.31	13.90	1.90	>99.0	0.22	0.04
J2203.2+1731	OY 101	FSRQ	LSP	1.076	34	2.83	1.29	5.49	1.28	>99.0	0.10	0.05
J2207.0−5347	PKS 2204−54	FSRQ	LSP	1.215	11	2.44	2.65	10.71	1.40	>99.0	1.17	0.24
J2229.8−0829	PKS 2227−08	FSRQ	LSP	1.560	41	3.71	1.40	7.05	1.16	>99.0	0.07	0.03
J2232.4+1141	CTA 102	FSRQ	LSP	1.037	43	3.10	1.50	9.11	1.34	>99.0	0.15	0.04
J2254.0+1609	3C 454.3	FSRQ	LSP	0.859	46	27.36	24.58	94.73	3.91	>99.0	0.82	0.02
J2325.3+3959	B3 2322+396	BLLac	LSP	...	20	2.07	1.33	5.32	1.34	>99.0	0.26	0.11
J2327.3+0947	OZ 42	FSRQ	LSP	1.843	42	3.05	2.12	13.67	1.39	>99.0	0.40	0.06
J2345.5−1559	PMN J2345−1555	FSRQ	LSP	0.621	19	2.29	0.93	4.47	1.03	69.3	0.02	0.06

Note. [a] Flux ($E > 300$ MeV) units: 10^{-8} photon cm^{-2} s^{-1}.

above three SED classes. These figures were obtained using only the 84 light curves with a coverage of $N_p/N_{\rm tot} \geqslant 60\%$. Variability amplitude of LSPs is generally larger than for ISPs and HSPs with the remarkable exception of the HSP source 0FGL J1218.0+3006 (ON 325, also known as Ton 605) which has the higher values of $F_M/\langle F\rangle$ among the LBAS sources (see also lower panel of Figure 9 for the maximum ratio of consecutive weekly flux values). This source was always close to the detection limit on a week timescale, but a strong flare was observed during 2009 October 10–15. This shows that although HSP seems to have, on average, a variability amplitude smaller than those observed in LSP, episodic large flaring activity can also be observed for this subclass of blazars.

Among the sources with a coverage <60% (22 sources), three sources have $F_M \sim 10^{-7}$ photon cm^{-2} s^{-1}. 0FGL J2207.0−5347 (PKS 2204−54) has a light curve dominated by a short and intense flare detected during 2008 September 3–8; 0FGL J1719.3+1746 (PKS 1717+177) was mainly active during 2008 September; 0FGL J0531.0+1331 (PKS 0528+134), one of the most active source during the EGRET era, was in a relative bright state during 2008 September–November, with two flaring episodes, it then decreased to a flux close to the *Fermi* LAT detection threshold on a week timescale.

To obtain an estimate of the time spent by each source in a bright state we evaluate the number of time bins (N_b) for which $(F_i - \sigma_i) > (\langle F\rangle + 1.5 \times S)$. The distribution of the ratio N_b/N in percent is reported in Figure 8. We see that high states exceeding one-fourth of the duration of the entire observation window are absent and that a very high number of sources were bright over a time interval shorter than the 5% of the total observation time. This distribution can be approximately described by a power law ($N_S = (382 \pm 107) \times (100 N_b/N)^{-1.9\pm0.2}$).

4. CHARACTERIZATION OF TEMPORAL VARIABILITY IN WEEKLY LIGHT CURVES

For the first time *Fermi* LAT is enabling a long-term view of high-energy source variability on a uniformly selected sample

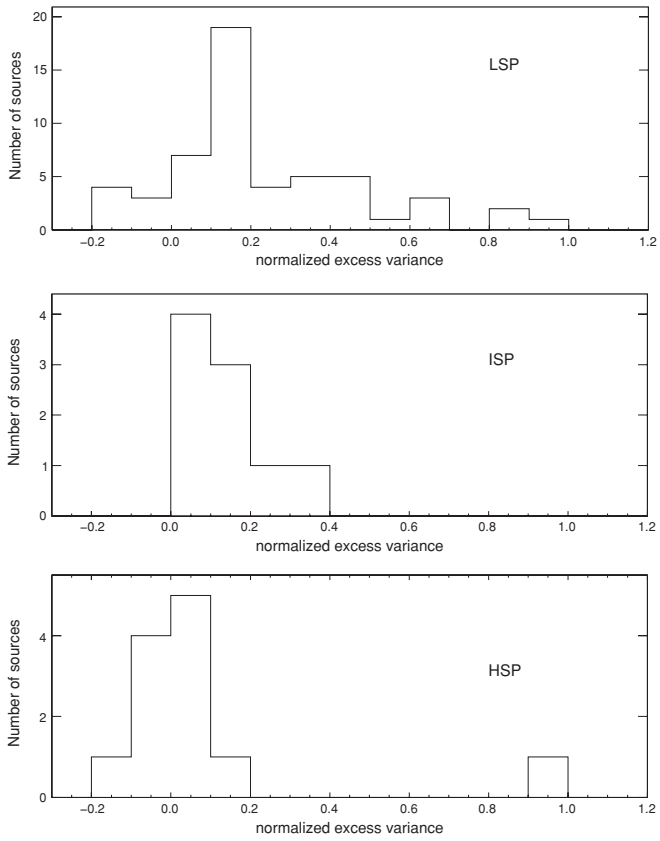

Figure 6. Distribution of the excess variance for the LSP, ISP, and HSP light curves with a coverage factor of $N_p/N \geqslant 60\%$.

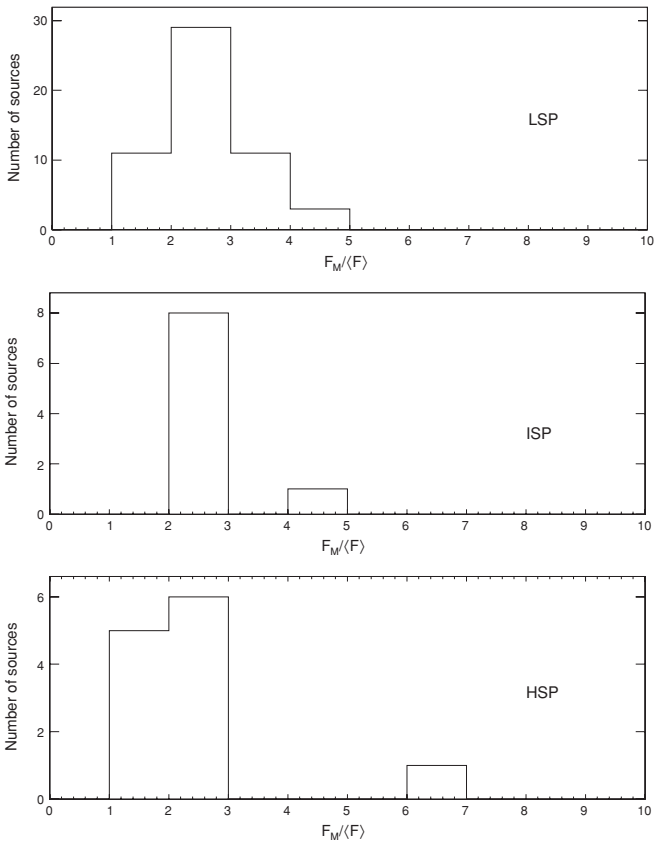

Figure 7. Distribution of $F_M/\langle F\rangle$ for the LSP, ISP, and HSP light curves with a coverage factor of $N_p/N \geqslant 60\%$.

of gamma-ray sources. In this section, we report the first and quantitative outlook to the 11 month weekly light curves shown in the previous section. As mentioned previously, 84 of the LBAS sources have at least 60% of the 47 weekly bins (at least 28 weekly bins) with TS $\geqslant 4$ flux detections (filled points in Figure 1). This allowed a quantitative time series analysis along the entire light curve (global analyses such as PDS or autocorrelation that are distinct from local analysis such as the flare shape analysis reported in Section 6, or wavelet analysis). In particular, the discrete auto correlation function (DACF) and the first-order SF are suitable methods to provide these first insights into fluctuation modes and characteristic timescales. To reduce contamination in results caused by the low brightness and non-variable sources that provide a white-noise contribution, a sub-sample of the 56 brightest and most variable objects is extracted from this list based on variability probability of χ^2 greater than 99% and normalized excess variance $\sigma^2_{\rm NXS} \geqslant 0.09$ (with exception of Mkn 421, 0FGL J1104.5+3811, and PKS 2155−304, 0FGL J2158.8−3014, taken into account because of their persisting level of flux over the entire period: see Figure 1, respectively, and Table 1).

In the upper panel of Figure 9, the scatter plot of the observed maximum of subsequent weekly flux variations versus the redshift (known for 53 of the 56 brightest and variable sources selected) is represented, for a comparison with the variable blazars seen during the EGRET era. The brightest blazars also showing the most apparent violent variations on weekly timescales, during these first 11 months of *Fermi* survey, are FSRQs PKS 1510−08 (Marscher et al. 2010; Abdo et al. 2010i), PKS 1502+106 (Abdo et al. 2010d), 3C 454.3 (Abdo et al. 2009c), 3C 279 (Abdo et al. 2010g), PKS 0454−234, and an ISP BL Lac object, 3C 66A. In a few cases, other sources historically classified as BL Lac objects showed rather violent gamma-ray variations, such as AO 0235+164 and BL Lacertae where flux increases approximatively around or above 10^{-7} photon cm^{-2} s^{-1}at $E > 300$ MeV.

In the lower panel of Figure 9, the observed maximum of the ratio of weekly flux values $F_{\rm high}/F_{\rm low}$ in subsequent time bins ($F_{\rm high}$ being the highest value in a pair of subsequent values both in case of increasing or decreasing trend) is plotted against the redshift. This plot points out a possible separation band between BL Lac objects and FSRQs. The transition region between the two families is roughly placed between redshift 0.5 and 1. In agreement with the results of Section 3 and the spectral results reported in Abdo et al. (2010b), the HSP BL Lac objects are well separated, being at the lowest redshift and least variable sources (with the exception of ON 325 as mentioned in the previous section). This ratio, being the relative flux change in subsequent weeks, is rather independent of redshift and more directly related to intrinsic dynamics, also points out different blazars as intrinsically violent variable sources, such as DA 55, B2 0716+33, OP 313, PKS 1454−354, and PKS 1329−049 (FSRQs), and also BL Lac objects such as ON 325 and W Com. This scatter plot shows that variability and redshift for AO 0235+164 fall into the FSRQs region, as confirmed by the physical properties of this source, more similar to that of an FSRQs than to that of a BL Lac.

The analysis of the DACF and SF techniques is applied to this same sample of the LBAS list. The DACF allows us to also investigate the level of autocorrelation in discrete data sets (see, e.g., Edelson & Krolik 1988; Hufnagel & Bregman 1992) without any interpolation and any invention of artificial data

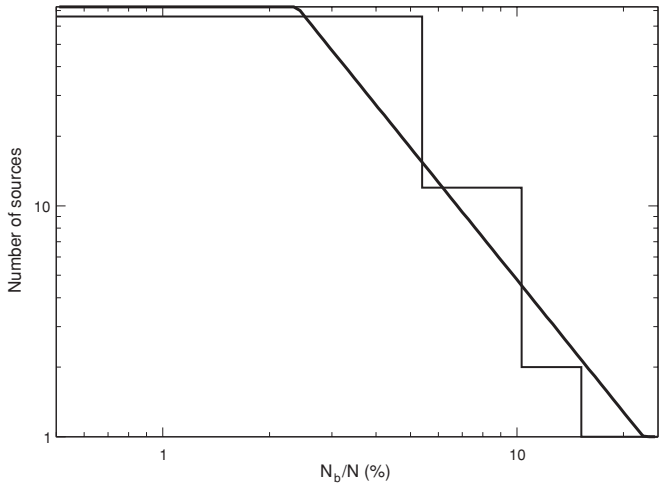

Figure 8. Distribution of N_b/N. This distribution could be described by a power law: $N_S = (382 \pm 107) \times (100 N_b/N)^{-1.9\pm0.2}$.

points. The pairs $[F(t_i), F(t_j)]$ of a discrete data set are first combined in *unbinned* discrete correlations

$$C_{ij}^{(u)} = \frac{(F_i - \langle F \rangle)(F_j - \langle F \rangle)}{\sigma_F^2}, \quad (3)$$

where $\langle F \rangle$ is the average values of the sample and σ_F is the standard deviation. Each of these correlations is associated with the pairwise lag $\Delta t_{ij} = t_j - t_i$ and every value represents information about real points. The DACF is obtained by binning the $C_{ij}^{(u)}$ in time for each lag Δt, and averaging over the number M of pairs whose time lag Δt_{ij} is inside Δt:

$$C(\Delta t) = (1/M) \sum_{ij} C_{ij}^{(u)}. \quad (4)$$

The choice of the bin size for irregular time series is governed by the trade-off between the desired accuracy in the mean calculation and the desired resolution in the description of the correlation curve. In this analysis, the bin is chosen equal to the sampling, 1 week, because of the limited temporal range and regularity (no gaps) of the light curves.

The SF is equivalent to the power density spectrum (PDS) of the signal calculated in the time domain instead of frequency space, which makes it less subject to sampling problems in the presence of very irregular time series, such as windowing and aliasing (see, e.g., Simonetti et al. 1985; Smith et al. 1993; Lainela & Valtaoja 1993; Paltani et al. 1997). This function represents merely a measure of the mean squared of the flux differences at times t and $t + \Delta t$ of N pairs with the same time separation Δt, along the whole time series. The first-order SF is defined as

$$\mathrm{SF}^{(1)}(\Delta t) = \frac{1}{N} \sum_{i=1}^{N} [F(t_i) - F(t_i + \Delta t)]^2, \quad (5)$$

where F_i is the discrete signal at time t. The general definition involves an ensemble average. This function is a sort of a "running" variance of the process that is able to discern the range of timescales that contribute to variations in the time series.

In the DACF and SF analysis of these 56 weekly LBAS light curves, true upper limits (TS < 1) are conservatively considered

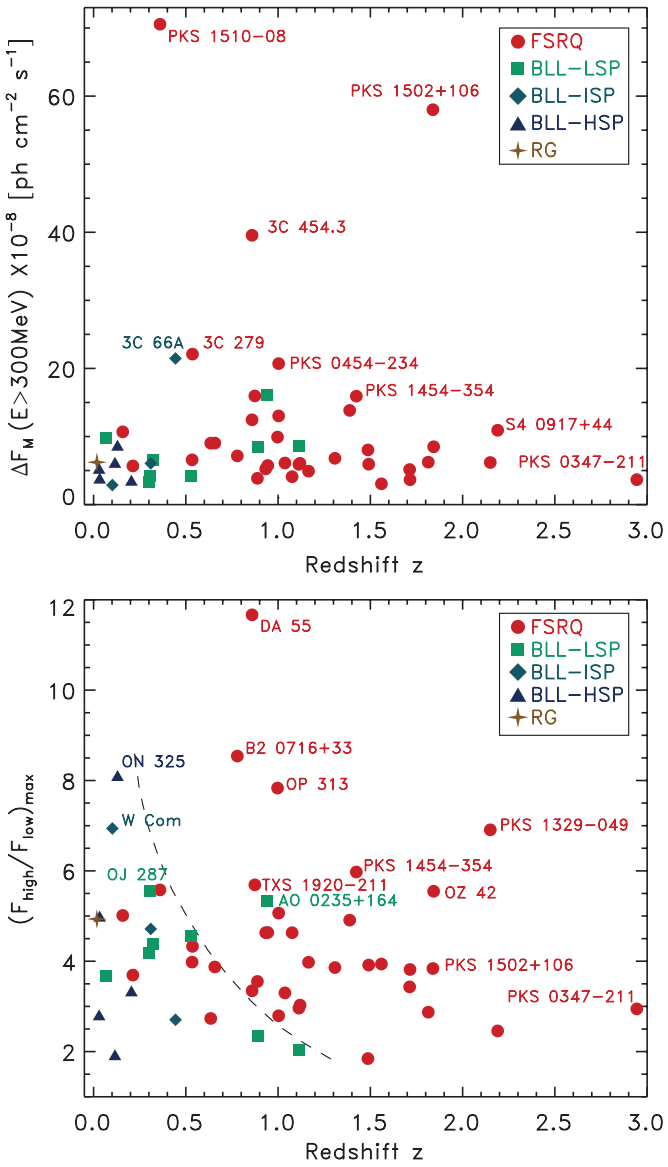

Figure 9. Upper panel: scatter plot of the observed maximum of flux variations ($F_{\rm high}/F_{\rm low}$) in adjacent weekly bins (variations for both flux increases or decreases in subsequent weeks) vs. the redshift for the 53 brightest and most variable sources of Table 1 with known z (or lower limit) and coverage $N_b/N \geqslant 60\%$. Most scattered sources are labeled, and different symbols and colors are used according to the classification of Table 1. Lower panel: scatter plot of the maximum ratio of flux variations in adjacent weekly bins vs. the redshift for the same sources. A possible separation band between BL Lac objects and FSRQs is indicated by the line.

(A color version of this figure is available in the online journal.)

as values close to zero (i.e., 10^{-12} photon cm^{-2} s^{-1}, well below the 11 month LAT sensitivity), avoiding in this way the bias of an underestimation of low flux states that a replacement with empty gaps of such bins would cause. The SF analysis performed on light curves, taking into account upper limits as explained above and, as a test, applied again on the same light curves with upper limits replaced by empty gaps, demonstrates a very low difference in results (about 80% of the sources show a difference in the calculated SF power-law index of ± 0.05).

Examples of 12 DACF and SF functions applied to these weekly light curves are reported in Figure 10. They show different autocorrelation patterns, and different central peak

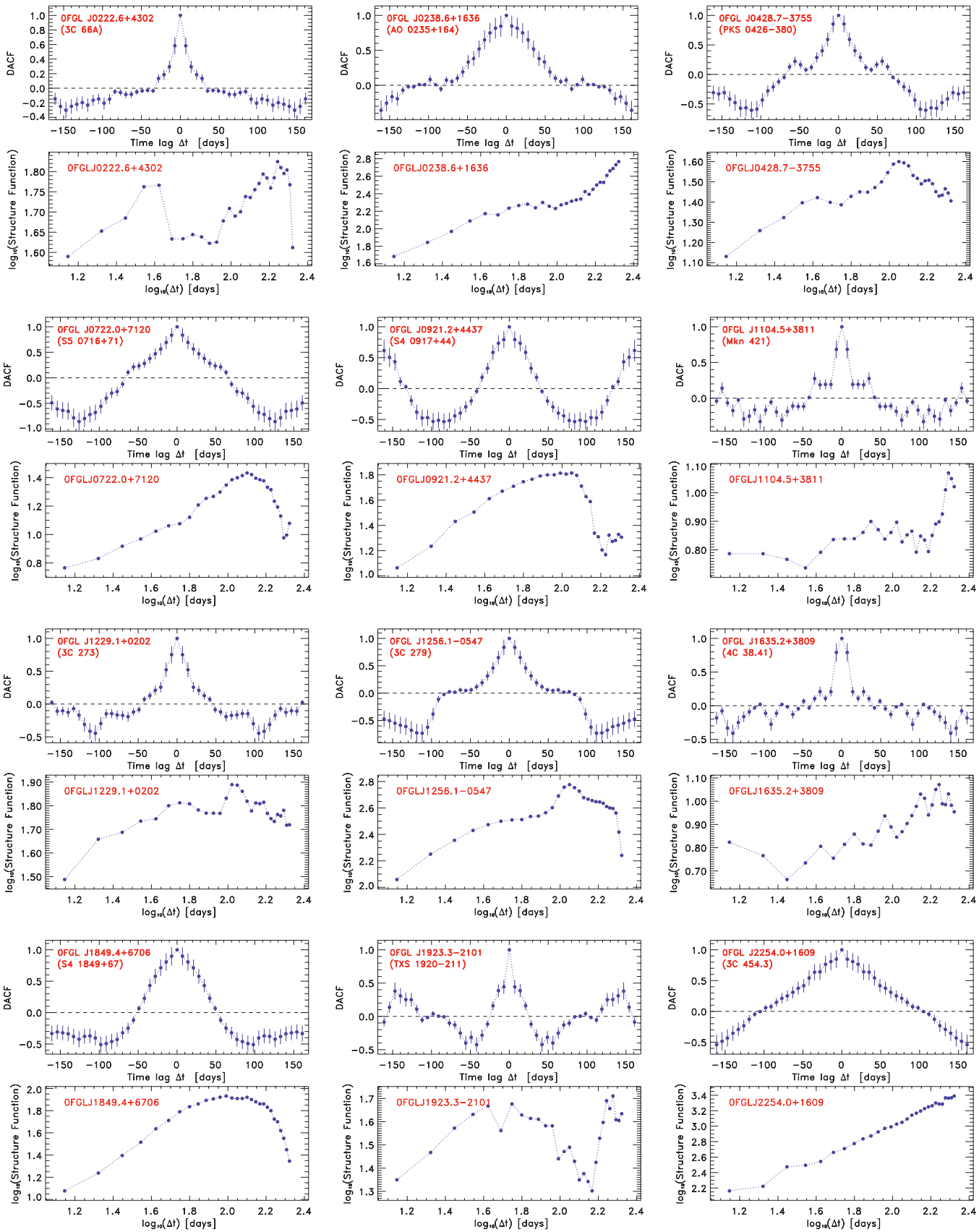

Figure 10. Example of DACF and SF functions applied to the weekly light curves of 12 LBAS blazars (from the left to bottom right: 3C 66A, AO 0235+164, PKS 0426−380, S5 0716+71, S4 0917+44, Mkn 421, 3C 273, 3C 279, 4C 38.41, S4 1849+67, TXS 1920+211, and 3C 454.3). They show different autocorrelation patterns, different zero lag peak amplitudes and crossing times, and different temporal power spectral trends and slopes, pointing out more different variability modes.

(A color version of this figure is available in the online journal.)

amplitude, and different temporal trends and slopes in logarithmic SF representation, pointing out different variability modes and timescales. The time lag $\Delta t_{\rm cross}$ where the DACF value crosses zero for the first time can indicate the maximum correlation scale, while equally spaced and repeated peaks in the function shape can point out characteristic timescales and hints for possible periodicity. Deep drops of the SF value can mean a small variance and provide again possible signature for a characteristic timescale. The ideal SF increases with the lag Δt in a log–log representation as in the plots shown in Figure 10. PDSs of blazars' light curves usually show power-law dependence on the signal temporal frequency f in a wide range of frequencies ($P(f) \propto 1/f^{\alpha}$). In case of sufficient sampling, sufficient total time range, and low noise, the SF can show a steep linear trend in a certain range of lags in logarithmic scale with index simply related to the PDS power index by $S \propto (\Delta t)^{\alpha-1}$ (Hughes et al. 1992; Lainela & Valtaoja 1993). If a maximum correlation timescale is reached in a light curve, the SF is constant for longer lags, and such a turnover point between the power-law portion and the constant trend can identify another important characteristic timescale. In real cases, the identification of a firm break in the SF and the fit of the trend is difficult and misleading because spurious features are common in these functions, resulting in a wiggling pattern and artificial breaks. These spurious features are systematic effects resulting from the finite length of the light curves, together with the random nature of the variability process itself (Emmanoulopoulos et al. 2010).

In Figure 11, we show four distributions of the power indices α evaluated through the SF applied in a blind mode to each of the 56 selected light curves from the minimum lag $\Delta t_{\rm min}$ of 1 week to a maximum lag $\Delta t_{\rm max}$ of 1/3, 1/2, 2/3, and 4/5 of the total time range $I(= t_{\rm max} - t_{\rm min})$. Most of the α values are distributed between 1.1 and 1.6, meaning a fluctuation mode about halfway between the pure flickering (also known as red noise, $\alpha = 1$) and the pure shot noise (also known as brown noise or Brownian variability, $\alpha = 2$, typically produced by a random walk process). Weaker sources, more affected by error dispersion, cause a whitening of the variability and shift the distributions closer to flickering, as well as the blind application of the SF when the maximum lag adopted is above the function break. For example, for the weekly light curve of 3C 279 the power index α estimated by the average of the four blind SF runs is 1.25, whiter than the value found when adopting $\Delta t_{\rm max} = (1/3)I$ only (well below the break) where we have a value of about 1.6 (Figure 11, top panel), in agreement with the value for the 3 day bin light curve found with the direct calculation of PDS analysis (Section 5).

These blind SF results at mid and long-term timescales appear roughly in agreement with the observed long-term optical variability based on some samples (for example optical spectral slope in the range 1.3–1.8 in Heidt & Wagner 1996; Webb & Malkan 2000; Fiorucci et al. 2003; Ciprini et al. 2007), and short-term X-ray variability (e.g., Green et al. 1993; Lawrence & Papadakis 1993; McHardy 2008). Radio light curves have power spectra with slopes around 2 in timescales from days up to several years (e.g., Hufnagel & Bregman 1992; Hughes et al. 1992; Lainela & Valtaoja 1993; Aller et al. 1999; Ciaramella et al. 2004; Hovatta et al. 2007; Nieppola et al. 2009).

The cases of 3C 454.3 (0FGL J2254.0+1609 a typical FSRQ) and AO 0235+164 (0FGL J0238.6+1636, LSP BL Lac object) are remarkable, showing, with weekly bin resolution, a full Brownian ($\alpha \gtrsim 1.8$) γ-ray variability with main monotonic baseline trends at long timescales, as depicted by the two outliers

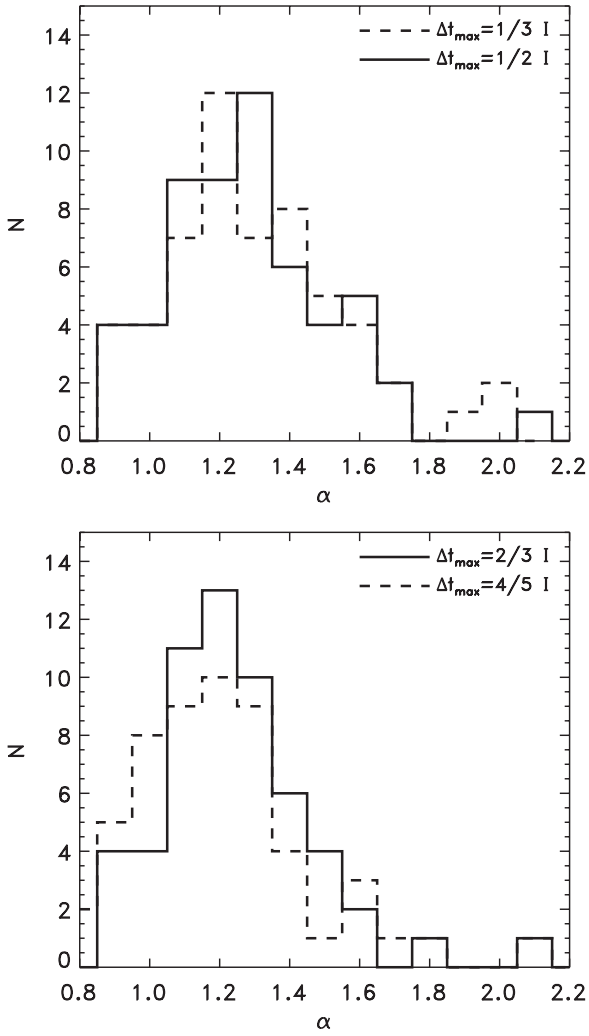

Figure 11. Distributions of the PDS power indices α for the weekly light curves of the 56 most bright and variable LBAS sources, selected as explained in the text. The values are obtained applying the SF considering four maximum lags (1/3, 1/2, top panel, and 2/3 and 4/5 bottom panel, of the total time range $I = t_{\rm max} - t_{\rm min}$). These distributions are peaked for values of the power index between 1.1 and 1.6.

of Figures 11 and 13 and as shown by the corresponding source light curves, the DACF and SF profiles of Figures 1 and 10.

In Figure 12, the DACF crossing times for the 53 brightest and variable sources (with known redshift or lower limit) are plotted against z. The distribution is reported as well. The most common $\Delta t_{\rm cross}$ values are from 4 to 13 weeks, pointing out the duration of the autocorrelation and therefore a possible characteristic timescale. The peak bin (nine sources) corresponding to 7 weeks (∼49 days) is likely associated with the periodic modulation in efficiency produced by the 55 day precession period of the *Fermi* spacecraft orbit (Abdo et al. 2010h). This is more evident for weakly variable sources such as Mkn 421 and W Com for example, even if intrinsic variability can in principle appear also at these timescales (as could be the case of 3C 273). Characteristic timescales can be better searched and quantified trough PDS using better sampled light curves for the subset of the brightest sources, as described in Section 5. In Figure 12 (lower panel), the DACF crossing times of the 15 LBAS sources that are also in the MOJAVE database are compared with the total apparent isotropic gamma-ray luminosity above 300 MeV

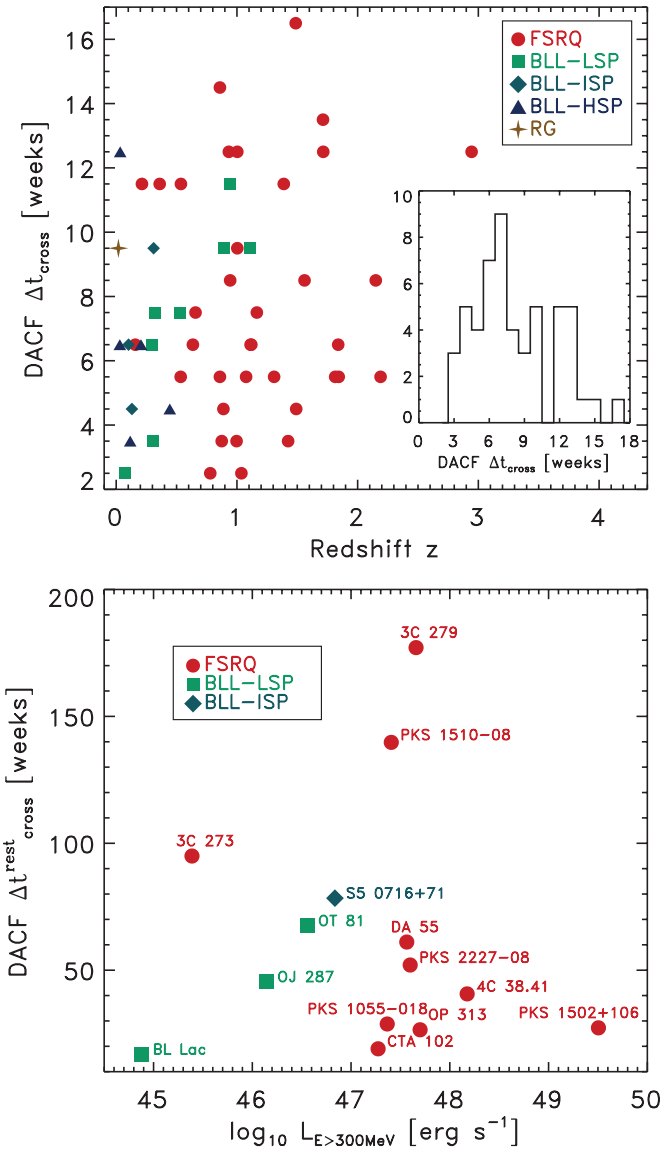

Figure 12. Upper panel: scatter plot of the DACF crossing times $\Delta t_{\rm cross}$ in weeks vs. the redshift for the 53 brightest and variable LBAS sources with known z (or lower limit). The inset reports the values distribution for the same set. Lower panel: scatter plot of the DACF crossing times in the rest frame of the source (corrected for z and beaming) vs. the total apparent isotropic γ-ray luminosity ($E > 300$ MeV) in the co-moving frame, defined as in the text, for 15 of the LBAS that are also part of the MOJAVE database. 3C 454.3 is out of the plot range (with $\Delta t^{\rm cross}_{\rm rest} = 254.3$ weeks and $\log_{10}(L_E) = 48.1$). All sources in this panel are labeled.

(A color version of this figure is available in the online journal.)

in the co-moving jet frame, defined as

$$L(E > 300\ \text{MeV}) = 4\pi d_L^2 \left(\frac{p-1}{p-2}\right)\left(\frac{\mathcal{D}}{1+z}\right)^{2-p} \cdot \quad (6)$$
$$\cdot\, E_{300} F(E > 300\ \text{MeV}),$$

where p is the gamma-ray photon index of the source spectrum modeled with a simple power law $dN/dE = N_0(E/1\ \text{GeV})^{-p}$ cm^{-2} s^{-1} MeV^{-1}, and d_L is the luminosity distance. Doppler factors $\mathcal{D}$ are taken from Hovatta et al. (2009) and Savolainen et al. (2010). In particular, PKS 1502+106 ($z = 1.8385$) showed the most intrinsically and isotropically luminous γ-ray outburst during these first 11 months of *Fermi* survey (for details, see Abdo et al. 2010d) and has a much

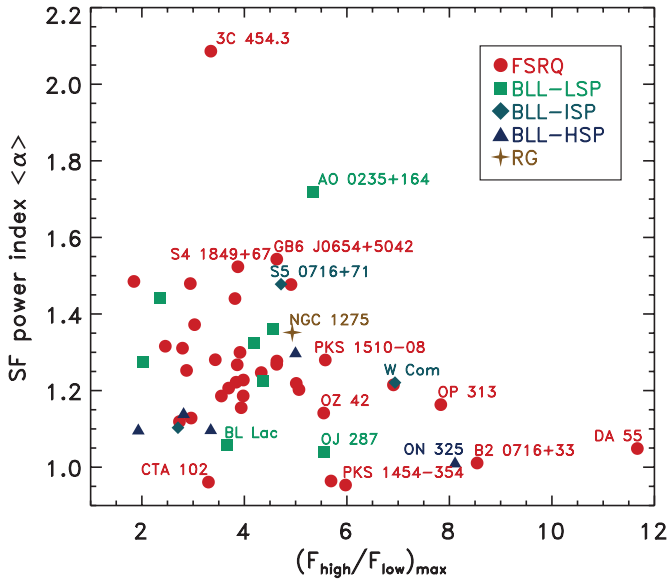

Figure 13. Scatter plot of the PDS power index α evaluated in time domain with the SF (averaged among the SF runs performed with four different maximum time lags, as reported in Figure 11) vs. the observed maximum of the week-to-week flux variations. Most scattered blazars are labeled.

(A color version of this figure is available in the online journal.)

shorter autocorrelation timescale with respect to the other two most powerful gamma-ray FSRQs, 4C 38.41 (S4 1633+38) and 3C 454.3 (Abdo et al. 2009c), of this period.

The values of α averaged over the four runs of the SF adopting the four different maximum lags mentioned, are reported for all the 56 sources in Figure 13 against the maximum of the subsequent week-to-week flux variations. In this case, a separation between FSRQs and BL Lacs is not evident, but the difference between the variability behavior of full Brownian gamma-ray sources such as AO 0235+164 and 3C 454.3 and the variability behavior of other powerful gamma-ray blazars such as PKS 1510-08 and PKS 1502+106 is clear. FSRQs such as PKS 1510-08 and PKS 1510+106 are characterized by more de-trended flares (departing from a constant baseline level) or by intermittence, while the most apparently bright FSRQs, like 3C 454.3, have clear long-term trends and stochastic long-term memory (i.e., high-order correlation structure meaning a persistent temporal dependence between observations widely separated in time and low-frequency dominated PDS).

In these weekly light curves no evident sign of periodicity is found, but a more detailed investigation of this aspect will be presented elsewhere using better sampled light curves over only the brightest blazars. In the following two sections, a global analysis (PDS) and a local analysis (functional fit of the flare temporal structure) are applied to more densely sampled light curves (3 day and 4 day bins, integrated flux $E > 100$ MeV) extracted only for the brightest 28 sources and 10 sources of the LBAS sample, respectively. These light curves starting from a lower energy threshold because of the high brightness and higher statistics are built as described in Section 2.

5. POWER DENSITY SPECTRA OF THE BRIGHTEST BLAZARS

In light curves with binning of a few days, about 15 of the sources are continuously, or almost continuously, detected throughout the 11 month period. For these 15 sources (9 FSRQs and 6 BL Lacs), we used light curves with 3 day binning and

for an additional 13 sources (all FSRQs) with slightly lower detection TS, we used light curves with 4 day binning. All light curves were evenly sampled without any data gaps, and a Fourier transform routine was used to compute PDSs.

The power density is normalized to fractional variance per frequency unit (rms^2 I^{-2} day^{-1}), and the PDS points are averaged in logarithmic frequency bins. The white noise level was estimated from the rms of the flux errors and was subtracted for each PDS.

In this section, we present the resulting PDS for a set of individual sources and also the averaged PDS for the two classes, FSRQs and BL Lacs.

There are a number of effects that can, potentially, distort the PDS of our analysis from the "true" long-term variability pattern. This includes stochastic variability within a finite length of observation, systematics in the data, and statistical noise. The last effect dominates at high frequencies so for the determination of PDS slopes we use primarily frequencies up to 0.02 day^{-1}.

The statistical (measurement) errors in the likelihood based light curves were investigated by simulations. These errors were also checked by comparing some light curves with corresponding ones obtained by direct aperture photometry, for which Poisson statistics is valid. This showed that the uncertainty in error estimates is not a significant problem for the brightest sources. For the less bright ones, including all the BL Lacs, this effect does introduce an uncertainty in the estimate of the white noise level in the PDS. The influence of this uncertainty on the PDS slope was estimated by repeating the analysis for a range of possible white noise levels and also by analysis of light curves extracted with different time bins (from 1 to 7 days).

Observational and instrument systematics were investigated by analyzing pulsar light curves extracted from the 11 month data with the same procedure as for the blazars. The most prominent effect is a periodic modulation that is identified with the 55 day precession period of the *Fermi* spacecraft orbit. This precession is consistent with the addition of the systematic error caused by the variation in effective area due to charged particles during orbital precession. This variation in the LAT effective area is a known effect that is caused by a change in exposure over the orbital precession period (Abdo et al. 2010h). In the PDS for individual blazars this peak is often hidden by the stochastic variability but does show up when averaging the PDS of a number of sources. The frequency bin at this period was not used when PDS slopes were estimated.

The PDS for some of the brighter sources are shown in Figure 14. The source to source differences are most likely dominated by the stochastic nature of the variability process and there is no significant evidence for a break in any of these cases.

To reduce the stochastic and statistical fluctuations and study the shape of the PDS for FSRQs and BL Lacs as groups, we averaged the PDS for each of these two classes using all sources detected with TS $>$ 4500. We do this under the assumption that the differences in PDS shape are small compared to the random fluctuations expected due to the action of the (presumed) underlying stochastic process. The resulting averaged PDS for the nine FSRQs is shown in Figure 15. The error bars are asymmetric 1σ errors for the mean over all sources and frequency points averaged in a logarithmic bin. To determine the PDS slope, we focus on the low frequency part, below 0.02 day^{-1}, since at higher frequencies the PDS is more sensitive to systematics due to uncertainties in the white-noise contribution. For frequencies below 0.017, we obtain a best-fit slope of 1.4 ± 0.1.

The averaged PDS for the six bright BL Lacs is similarly fitted with a power law up to 0.017 day^{-1}. This gives a slope of 1.7 ± 0.3 with white noise based on the light curve errors. The sample of sources consists of three LSP's (AO 0235+164, PKS 0426−380, and PKS 0537−441), one ISP (3C 66A), and two HSP's (Mkn 421 and PKS 2155−304). Due to the stochastic nature of the variability and the fact that few sources are considered, it is difficult to draw firm conclusions about the differences between the low- and high-peaked BL Lacs. An indication of a trend, however, is that the three LSP's show stronger variability at longer timescales and therefore dominates the determination of the average, steep slope while the two HSP's both have PDS slopes flatter than 1.0. Further observations are needed to see if this trend can be firmly established.

To increase the data sample and to test if source brightness affects the analysis we selected the remaining FSRQs with TS $>$ 1000 and extracted light curves with a 4 day binning. Sources where parts of the light curve had very large flux errors were not used. This resulting sample consisted of 13 sources for which the PDS was averaged and analyzed in the same way as for the brightest sources. For this PDS, we obtain the best-fit slope of 1.5 ± 0.2 in good agreement with the slope for the first sample.

Figure 15 shows all three averaged PDS together for comparison. The difference in the PDS slope for BL Lacs and FSRQs is of marginal significance but we note that the BL Lac slope is consistent with 2 while this is not the case for the FSRQs. None of the averaged PDS shows any significant evidence for the presence of a break although this may still not be excluded for individual sources. From Figure 15 it is also evident that for the present data the fractional variability of the BL Lacs is less than that of the FSRQs, at least up to the 54 day satellite precession peak. The total fractional rms integrated up to 0.017 day^{-1} in the PDS for the nine FSRQs is 1.35 times that of the six BL Lacs. If the ratio is instead estimated by dividing the PDS for the two groups point by point (which gives equal weight to each frequency point), we get a value of 1.5. Both estimates were made after subtraction of a white noise level corresponding to the flux error values. If the actual white noise level is larger than this, the ratio between the FSRQ and BL Lac fractional variance is most likely larger than our estimate here.

6. TEMPORAL STRUCTURE OF FLARES FOR THE BRIGHTEST BLAZARS

The analysis of individual flares is performed using the extracted 3 day time bin flux (E $>$ 100 MeV) light curves (except for PKS 1502+106 for which we chose 7day time bins), as described in Section 2. For this analysis, we selected the light curves of the 10 sources that exhibited high variability with several flares either separated or partially superimposed (see Table 2.

We use the following function to reproduce the time profile of a single flare:

$$F(t) = F_c + F_0 \left(e^{\frac{t_0 - t}{T_r}} + e^{\frac{t - t_0}{T_d}} \right)^{-1}, \quad (7)$$

where F_c represents an assumed constant level underlying the flare, F_0 measures the amplitude of the flares, t_0 describes approximatively the time of the peak (it corresponds to the actual maximum only for symmetric flares), and T_r and T_d measure

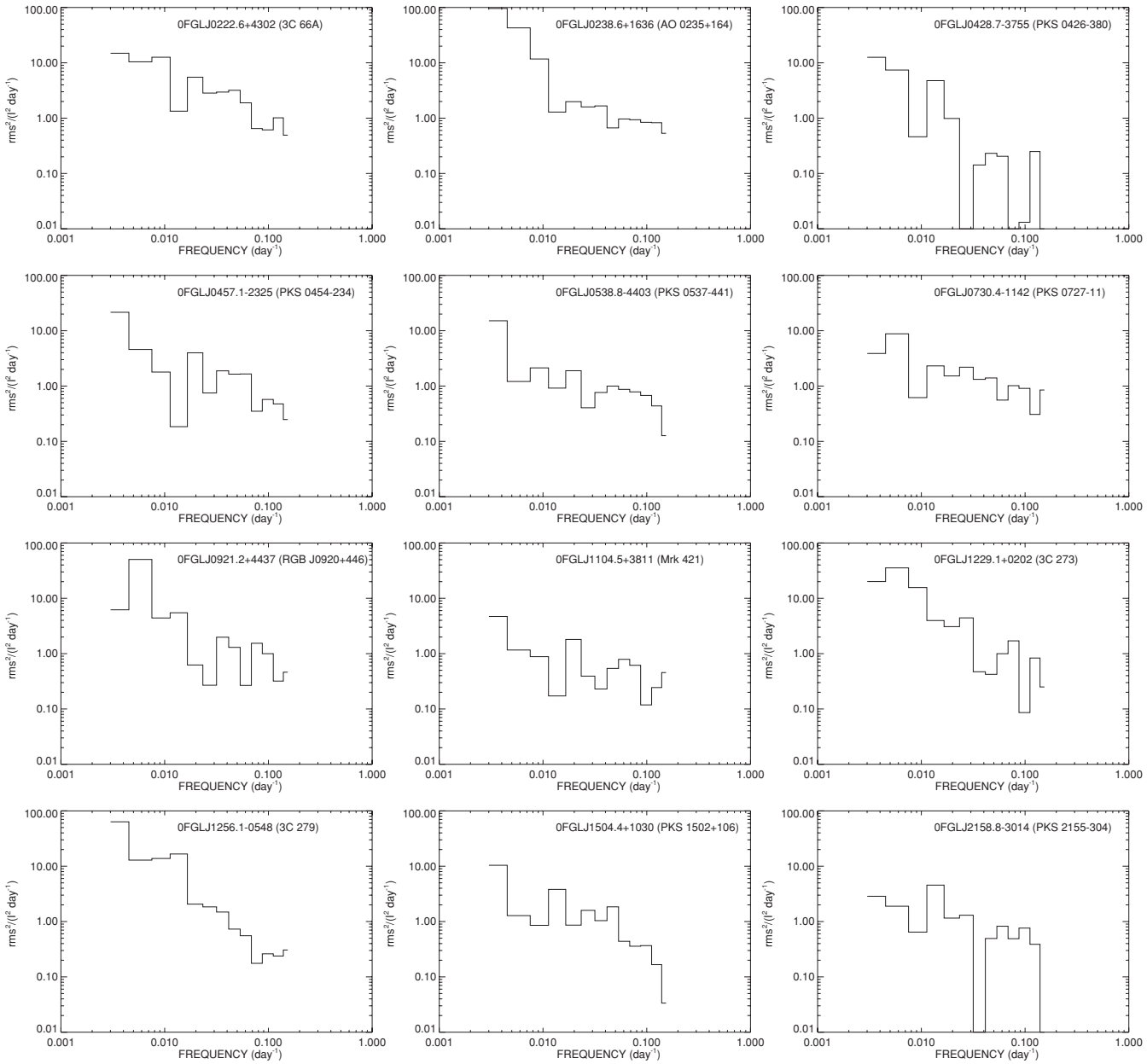

Figure 14. Power density spectra computed from 3 day binned light curves for some of the brighter sources. The power density is normalized to $\mathrm{rms}^2\ I^{-2}\ \mathrm{day}^{-1}$ and the estimated white noise level has been subtracted.

the rise and decay time. This function is well suited to study both the duration and symmetry of the individual flares. Double exponential forms for the functional fit were used in the past to fit individual blazar flare pulses (Valtaoja et al. 1999). Other and more general functions are used in gamma-ray burst science (see, for example, Norris et al. 2000, 2005; Vetere et al. 2006). The time of the maximum of a flare can be easily computed from the first derivative of Equation (7):

$$t_m = t_0 + \frac{T_r T_d}{T_r + T_d} \ln\left(\frac{T_d}{T_r}\right), \tag{8}$$

which is equal to t_0 for $T_d = T_r$. A good estimate of the total duration of the flare is

$$T_{fl} \simeq 2(T_r + T_d), \tag{9}$$

which, for symmetric flares, corresponds to the interval where the flux level is reduced to about 20% of the peak value.

As a first step, we identify the flare to be fitted and detect the time of the peak, which was kept frozen in the fitting procedure unless the flare was clearly superimposed on to a slow trend. We build a function with as many components as the flares' number and perform a fit for each source with the function of Equation (7). To verify the validity of this procedure, we analyzed the distribution of the residuals, calculated by subtracting the observed flux from the modeled one and dividing by the flux errors, which should be compatible with a constant level. Figure 16 shows the light curves of six sources with the fit function superimposed, 3C 66A, PKS 0426−380, PKS 0454−234, 3C 273, 3C 279, and 3C 454.3. This procedure was satisfactory for the majority of the flares, but for a few events it did not provide quite good fits. For instance, in the case of the first flare 3C 273 some data points lie above the fitting curve and this discrepancy could be due to events of short duration which were not well sampled.

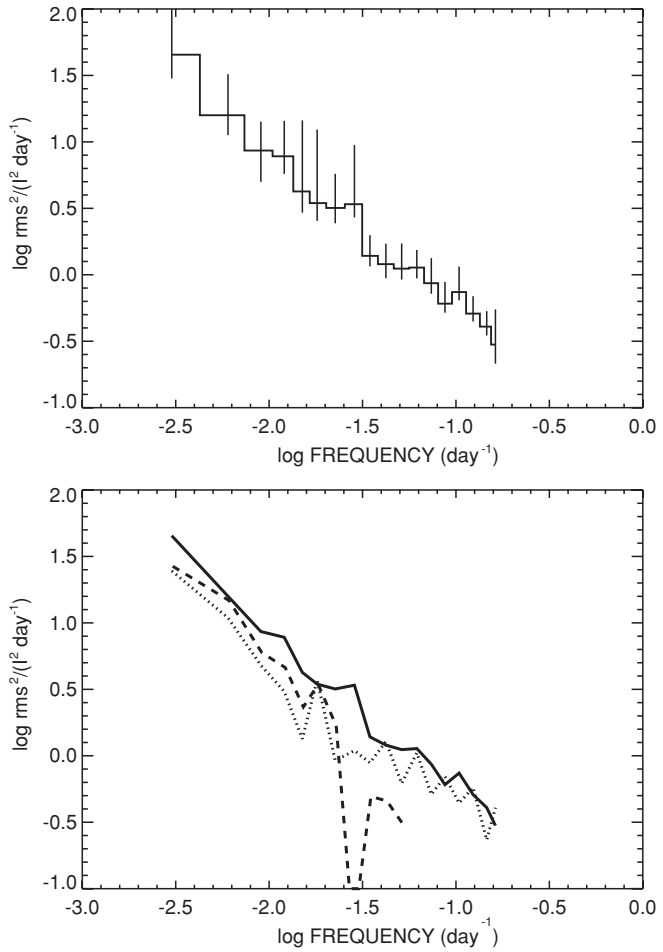

Figure 15. Top: average power density spectrum (PDS) for the nine brightest FSRQs. White noise level based on light curve error estimates has been subtracted. The error bars are asymmetric 1σ errors of the mean. Our best-fit estimate is a PDS slope of 1.4 ± 0.1. Lower: a comparison of the averaged PDS for three sets of sources, the 9 bright FSRQs from the upper plot (solid line), the 6 brightest BL Lac's (dotted line) and 13 additional FSRQs with TS > 1000 (dashed line). Best-fit slope for the BL Lac and fainter FSRQs is 1.7 ± 0.3 and 1.5 ± 0.2, respectively.

We also defined the following parameter to describe the symmetry of the flares:

$$\xi = \frac{T_d - T_r}{T_d + T_r}, \tag{10}$$

which spans between -1 and 1 for completely right and left asymmetric flares, respectively.

The value of ξ can provide a useful indication of the physical evolution of the flare. Those having a marked asymmetric profile can be explored in terms of a fast injection of accelerated particles and a slower radiative cooling and/or escape from the active region. Symmetric flares, with or without a long standing plateau, can be related to the crossing time of radiation (or particles) through the emission region or can be the result of the superposition of several episodes of short duration. The ξ parameter is used to define three different classes of flares: (1) symmetric flares where $-0.3 < \xi < 0.3$, (2) moderately asymmetric flares when $-0.7 < \xi < -0.3$ or $0.3 < \xi < 0.7$, and (3) markedly asymmetric flares when $-1.0 < \xi < -0.7$ or $0.7 < \xi < 1.0$. The parameters are listed in Table 2, and their distributions are shown in Figure 17.

We also calculated the weighted mean of these parameters to study the general properties of the time profiles of gamma-ray flares. We obtain $\langle \xi \rangle = -0.084 \pm 0.009$ and $\langle T_{fl} \rangle = 11.87 \pm 0.12$. Looking at the results of the fitting procedure and the weighted means we can see that the list of brighter sources shows two different types of temporal profiles: the sources with a stable baseline with a sporadic flaring activity and the sources with a strong activity with complex and structured features. Based on our analysis we can put 3C 66A, PKS 0426−380, S4 0917+44, and PKS 0454−234 in the first class of objects and 3C 279, 3C 273, 3C 454.3, PKS 1502+106, AO 0235+164, and PKS 1510−08 in the second one, while no evidence of very asymmetric profiles is found. In Figure 16, we report cases of both classes to show the different time profiles. Note that for the majority of events the uncertainties on ξ are small; however, for a few flares of 3C 66A, AO 0235+164, and PKS 0454−23, the resulting asymmetries are not safely estimated. In fact, despite their large values the occurrence of symmetricity in moderately asymmetric profiles cannot be excluded within 1 standard deviation.

We found only four markedly asymmetric flares: for 3C 66A (DoY 2008 260 $\xi = 0.73 \pm 0.30$), 3C 273 (DoY 2008 340 and 445, $\xi = 0.88 \pm 0.04$ and $\xi = -0.76 \pm 0.04$, respectively), and PKS 1502+106 (DoY 2008 305, $\xi = -0.71 \pm 0.12$), where two of them have rise times longer than the decays. In the case of 3C 66A, the flare was rather short and the resulting uncertainty on ξ is large; therefore no firm conclusion on its shape can be established. The two flares of 3C 273 clearly exhibit different profiles. Note that the highest point of flare at epoch 340 is well above the fitting curve implying the possibility of an even higher value of ξ, whereas the subsequent and much longer flare (DoY 2008 445), which has a very well established negative asymmetry, may be due to confusion because of the partial superposition of low amplitude and short events, not individually detectable. 3C 273 also exhibited a couple of exceptional flares in 2009 September (Abdo et al. 2010f) in which it reached a very high level, and the light curves were very finely sampled. In both episodes rise times were shorter than the subsequent decays. Similarly, PKS 1502+106 exhibited a markedly asymmetric outburst in 2008 August, resolved with a daily binning (Abdo et al. 2010d).

7. SUMMARY AND CONCLUSIONS

Gamma-ray light curves (Figures 1 and 2) and variability properties of the 106 LBAS blazars (0FGL list; Abdo et al. 2009a, 2009b) collected during the first 11 months of the all-sky survey by *Fermi* LAT are presented. This represents a first systematic study of gamma-ray variability over a consistent set of homogeneously observed blazars.

The light curves of 84 of these sources have at least 60% of the 47 weekly bins with flux detection of TS > 4 ($\gtrsim 2\sigma$), and 56 have also a significant excess variance (Table 1). The low gamma-ray brightness states interposed among the flares are studied, for the first time as well, and high flux states do not exceed 1/4 of the total light curve range (most sources being active in periods shorter than 5% of the total light curve duration). FSRQs and LSP/ISP BL Lac objects showed the largest variations, as expected, with the high energy SED component peaked at MeV and GeV bands. HSP BL Lac object shows lower variability (with remarkable exception of ON 325), and their emission is persistent, easily detected in all the weeks of the considered period, and also because of their smaller redshift (Section 3).

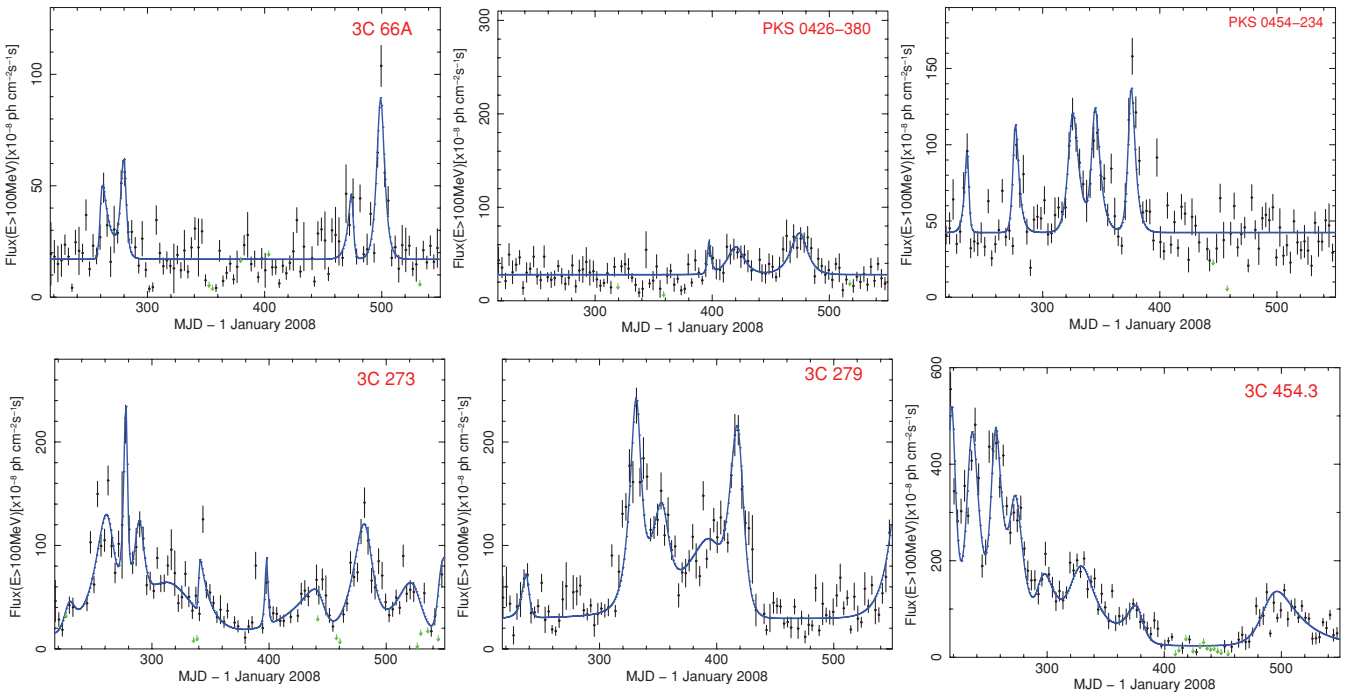

Figure 16. Six representative light curves ($E > 100$ MeV) of bright blazars (3C 66A, PKS 0426−380, PKS 0454−234, 3C 273, 3C 279, and 3C 454.3) obtained with 3 day bins. Data points represent detected flux values having a TS greater than 9, and the continuous (blue) curve represents the best-fit function described in Equation (7).

(A color version of this figure is available in the online journal.)

In these first 11 months of *Fermi* mission, PKS 1510−08, PKS 1502+106, 3C 454.3, 3C 279, and PKS 0454−234 (all FSRQs) are observed to be the brightest and most violently variable gamma-ray blazars. In a few cases this was also true for BL Lac objects (3C 66A and AO 0235+164 for example). In particular, PKS 1502+106 (OR 103), 4C 38.41 (S4 1633+38), and 3C 454.3 were also the most intrinsically gamma-ray powerful blazars in these months. The other sources appear distributed with decreasing observed subsequent maximum variations with increasing redshift. Different autocorrelation patterns, central lag peak amplitudes, zero crossing times, different temporal trends, and power-law indices are shown by the DACF and SF, pointing out different timescales and variability modes (more flicker-dominated or Brownian-dominated). The weekly PDSs evaluated using the SF in blind mode point out a $1/f^{\alpha}$ trend with α values mostly distributed between 1.1 and 1.6. Light curves of AO 0235+164 and 3C 454.3 are observed to be fully Brownian (i.e., with the steepest PDS slopes, $\alpha \geqslant 2$) with longer emission cycles and sustained flares that could identify more massive central black holes. Other powerful sources such as PKS 1510−08 and PKS 1510+106 show variability behavior half-way between the two classes above (with $\alpha \sim 1.3$), showing intermittence and de-trended complex superposed flares, respectively. The DACF crossing lag times are found mostly distributed between 4 and 13 weeks with a peak at 7 weeks.

The mean variability properties for the brighter sources are studied in more detail by calculating an average PDS for each of the two main blazar types, FSRQs (nine sources) and BL Lacs (six sources). For both types, the average PDS is described by a power law without any evidence of a break in the frequency range where our sensitivity is best (0.003 to at least 0.017 day^{-1}). The power-law index for the averaged PDS was estimated to be 1.4 ± 0.1 and 1.7 ± 0.3 for the FSRQs and BL Lacs, respectively. The BL Lac sources show a large spread in PDS slopes with an indication of trend such that the PDS is steeper for LSPs than for the HSPs. Further observations are needed to establish this trend, but we note that in the present data the two brighter HSP's (Mkn 421 and PKS 2155−304) have PDS slopes of order 1 or flatter. For Mkn 421, we can compare this with the corresponding result for soft X-rays. Analyzing the RXTE ASM X-ray light curve for this source, we obtain a well-defined power-law index of 1.04 ± 0.05. Aside from Mkn 421, the best available long-term X-ray light curve is that of the FSRQ 3C 279. For this source, Chatterjee et al. (2008) found a slope of 2.3 ± 0.3 for the X-ray band and 1.7 ± 0.3 for the optical. In this case our result in the gamma-ray band, both the average for FSRQs and for 3C 279 itself (1.6 ± 0.2), is closer to the PDS slope in the optical than in X-rays. More generally, the gamma-ray PDSs of the bright *Fermi* LAT sources have slopes similar to those obtained from long-term optical and radio light curves (Section 4). For the X-ray band, the situation is less clear since only a few sources have good enough long-term light curve to allow for a comparison.

The power density excess (above the noise level) in the 0.003–0.017 day^{-1} range was found to correspond to a mean rms fractional variability (rms/I^2) of 0.50 for the nine bright FSRQs and 0.37 for the six brightest BL Lacs. These results imply that in the LAT energy range and presently accessible timescales the FSRQs exhibit a larger relative variability than the BL Lac's.

Gamma-ray variability observed in these LBAS blazars can be described both as essentially steady sources with perturbations or as a series of discrete, though possibly overlapping, flares produced, for example, by traveling shock fronts. The emission could be produced in multiple regions forming an inherently inhomogeneous blazar zone or in an essentially homogenous region where all particles are accelerated, depending on the particular source considered.

Table 2
Flare Structure Fit for 3 Day Bin Light Curves of the Brightest Blazars

3C 66A flare_time[a]	$\chi^2_r = 8.0$ ξ	T_{fl}[b]
260	0.73 ± 0.30	14.7 ± 11.9
280	−0.19 ± 0.19	8.3 ± 1.7
475	−0.55 ± 0.33	8.8 ± 2.5
495	0.02 ± 0.67	11.8 ± 7.9
Average	0.003 ± 0.207	10.88 ± 3.6
AO 0235+164 flare_time[a]	$\chi^2_r = 11.4$ ξ	T_{fl}[b]
230	0.16 ± 0.07	21.7 ± 1.5
251	0.61 ± 0.06	34.4 ± 1.5
291	−0.49 ± 0.11	24.0 ± 1.9
301	0.63 ± 0.43	21.1 ± 7.9
380	0.04 ± 0.13	63.9 ± 8.3
401	0.36 ± 0.09	6.3 ± 0.5
425	0.55 ± 0.18	47.3 ± 7.2
460	−0.04 ± 0.38	19.1 ± 7.4
485	−0.17 ± 0.08	5.4 ± 0.4
Average	0.18 ± 0.07	27.02 ± 1.74
PKS 0426−380 flare_time[a]	$\chi^2_r = 2.2$ ξ	T_{fl}[b]
395	0.10 ± 0.07	4.4 ± 0.3
420	0.01 ± 0.30	24.2 ± 7.4
475	−0.11 ± 0.07	25.2 ± 1.8
Average	0.0003 ± 0.1068	17.97 ± 2.52
PKS 0454−23 flare_time[a]	$\chi^2_r = 5.0$ ξ	T_{fl}[b]
236	−0.39 ± 0.10	6.6 ± 0.5
276	0.33 ± 0.24	9.0 ± 2.2
325	0.21 ± 0.08	16.0 ± 1.2
344	0.30 ± 0.63	13.0 ± 7.9
375	0.25 ± 0.78	10.9 ± 8.2
Average	0.14 ± 0.21	11.07 ± 2.34
S4 0917+44 flare_time[a]	$\chi^2_r = 9.4$ ξ	T_{fl}[b]
364	0.0001 ± 0.1650	120.1 ± 19.8
520	0.0001 ± 0.0707	80.1 ± 5.6
Average	0.0001 ± 0.0898	100.10 ± 10.29
3C 273 flare_time[a]	$\chi^2_r = 3.7$ ξ	T_{fl}[b]
229	0.13 ± 0.07	15.8 ± 1.1
263	−0.32 ± 0.03	30.2 ± 1.3
278	−0.24 ± 0.08	6.1 ± 0.4
290	−0.22 ± 0.17	15.5 ± 2.2
340	0.88 ± 0.04	17.0 ± 0.4
398	−0.11 ± 0.07	4.5 ± 0.3
445	−0.76 ± 0.04	68.0 ± 1.5
483	−0.31 ± 0.09	30.7 ± 2.3
525	−0.46 ± 0.11	45.7 ± 3.6
Average	−0.16 ± 0.03	25.93 ± 0.89
3C 279 flare_time[a]	$\chi^2_r = 3.7$ ξ	T_{fl}[b]
238	−0.33 ± 0.24	11.0 ± 2.3
332	−0.22 ± 0.08	17.0 ± 1.2
355	−0.41 ± 0.03	28.4 ± 1.3
398	−0.67 ± 0.05	71.9 ± 4.2
419	0.29 ± 0.08	22.4 ± 1.6
Average	−0.27 ± 0.05	30.11 ± 1.07
PKS 1502+106 flare_time[a]	$\chi^2_r = 4.4$ ξ	T_{fl}[b]
242	−0.20 ± 0.10	40.7 ± 3.8
305	−0.71 ± 0.12	41.6 ± 2.9
336	0.11 ± 0.11	31.6 ± 3.2
365	0.13 ± 0.14	21.3 ± 3.4
405	0.28 ± 0.09	55.6 ± 4.1
485	−0.18 ± 0.08	57.2 ± 4.1
525	−0.05 ± 0.07	36.8 ± 2.6
Average	−0.09 ± 0.04	40.67 ± 1.31
PKS 1510−08 flare_time[a]	$\chi^2_r = 17.8$ ξ	T_{fl}[b]
260	−0.52 ± 0.12	25.1 ± 2.0
381	−0.39 ± 0.10	19.7 ± 1.5
445	0.07 ± 0.01	24.2 ± 0.3
480	0.25 ± 0.08	11.1 ± 0.8
Average	−0.15 ± 0.04	20.00 ± 0.66
3C 454.3 flare_time[a]	$\chi^2_r = 7.3$ ξ	T_{fl}[b]
235	0.24 ± 0.16	20.3 ± 3.8
255	0.29 ± 0.08	18.0 ± 1.3
272	0.24 ± 0.36	22.2 ± 7.9
295	0.44 ± 0.28	32.2 ± 8.2
327	0.25 ± 0.13	41.8 ± 4.4
378	−0.42 ± 0.10	28.5 ± 2.2
490	0.48 ± 0.11	59.4 ± 4.7
Average	0.22 ± 0.07	31.79 ± 1.98

Notes.
[a] Day of the flare peak (DoY 2008 unit).
[b] Fraction of days.

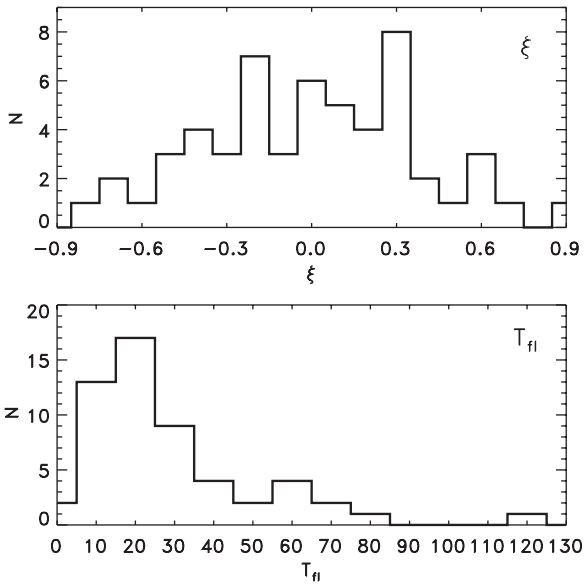

Figure 17. Distributions of the flare pulse parameters for the cumulated 10 bright blazars analyzed with this technique. Values of ξ above and T_{fl} below are shown.

Random walk processes producing such PDS variability slopes, such as instabilities and turbulence in the accretion flow through the disk or in the jet, can cause the intermittent behavior observed in several of these *Fermi* LAT light curves. These are stochastic processes, mostly characterized by the presence of a large number of weakly correlated elements

which appear at random, live only a short time, and decay. Steep PDS slopes mean more Brownian-dominated regimes characterized more by long memory and self-similarity. Large flares likely arise from the sudden acceleration of relativistic electrons, related to bulk injections of new particles and/or strong internal shocks (Mastichiadis & Kirk 1997; Spada et al. 2001; Böttcher & Dermer 2010). These type of PDSs could be related to mass accretion avalanches providing shot pulses: larger (and longer) shots contribute to the low-frequency part of the PDS, while smaller and shorter shots determine the power law decline at high frequencies. In this case, variability would be explained as disturbances or inhomogeneities in the accretion process, opposite to intermittence, which can be evidence of dissipation in the jet and described by turbulence-driven processes. Furthermore, well identified GeV recurrent characteristic timescales, pointed out by breaks in the PDS, can be related linearly to the mass of the central supermassive black hole (Markowitz 2006; Dermer 2007; Wold et al. 2007; McHardy 2008), as happens for X-ray variability timescales in Seyfert galaxies, but more detailed analysis with improved sampling is needed to shed light on this issue.

Finally, the local analysis of flare temporal shapes for the brightest sources revealed and confirmed in a quantitative way different temporal profiles: stable baseline with sporadic flaring activity or strong activity with complex and structured temporal features. The average durations of the fitted flares varied from about 10 days up to 100 days in the case of S4 0917+44. In other very bright flares, timescales as short as a fraction of a day have been observed (3C 273, PKS 1510−089) and in some cases the light curves were structured in a series of shorter peaks. The low mean asymmetry of the events analyzed in Section 6 can be then explained by the superposition of a series of peaks, even if the light curves analyzed are already resolved with a short, 3 day sampling. A marked asymmetric profile can be explained in terms of a fast injection of accelerated particles and a slower radiative cooling and/or escape from the active region and could be considered cooling-dominated flares. The fast rise and slower decay can be evidence for a dominant contribution by Comptonization of photons produced outside the jet (Sikora et al. 2001). Gamma-ray flares produced by short-lasting energetic electron injections and at larger jet opening angles are predicted to be more asymmetric showing much faster increase than decay, the latter determined by the light travel time effects. On the other hand, symmetric flares, with or without a long standing plateau, can be related to the crossing time of radiation (or particles) through the emission region, dominated by geometry and spatial scales (Takahashi et al. 2000; Tanihata et al. 2001). Flares observed at or above the peak energy reflect the scale of the source along the line of sight and are symmetric in the cylindrical geometry of the active regions (Eldar & Levinson 2000; Sokolov et al. 2004). The result of the superposition and blending of several episodes of short duration could also provide symmetric flare shapes (Valtaoja et al. 1999).

The presentation of gamma-ray light curves of a consistent set of blazars observed in homogeneous conditions by *Fermi* LAT over almost one year, and our systematic variability characterization showed properties in some ways similar to the radio-band and optical variability. Variation amplitudes, flare durations, PDS slope values, preliminary hints for typical timescales, and morphology of the flares can be used to support the identification of the correct source class for newly discovered unidentified sources. Basically, an LAT gamma-ray blazar is displaying two "flavors" of variability: a rather constant baseline with sporadic flaring activity showing also intermittence and characterized by flatter PDS slopes resembling the red noise, flickering, fluctuations, and a few sources showing strong activity with complex and structured time profiles characterized by the long memory and steeper PDS slopes of random walk processes. Finally, our results can also serve as a preparatory study for more detailed analysis and modeling that are possible with the brightest and most variable sources through better sampling and time resolution.

Table 3
Tabulated Data of the Weekly Flux Light Curves Reported in Figures 1 and 2

0FGL name	Weekly Index[a]	Flux ($E > 300$ MeV) [10^{-6} photons cm^{-2} s^{-1}]	Error	TS	Upper Limit
J0017.4-0503	0	0.0565	0.0107	64.2	0.0000
J0017.4-0503	1	0.0141	0.0067	7.5	0.0291
J0017.4-0503	2	0.0158	0.0072	10.3	0.0293
J0017.4-0503	3	0.0514	0.0109	49.5	0.0000
J0017.4-0503	4	0.0276	0.0107	11.1	0.0470
J0017.4-0503	5	0.0265	0.0090	15.8	0.0428
J0017.4-0503	6	0.0330	0.0099	20.3	0.0506
J0017.4-0503	7	0.0276	0.0084	24.6	0.0426
J0017.4-0503	8	0.0089	0.0052	6.6	0.0189
J0017.4-0503	9	0.0278	0.0088	18.2	0.0437

Notes. [a] The relation between weekly index and time is as follows. The week with index 0 begins on Aug. 5, 2008 at 00:00:00 UTC, MJD 54683, MET 239587200, so the week with index i begins on MJD 54683+7xi and ends on MJD 54690+7xi.

(This table is available in its entirety in a machine-readable form in the online journal. A portion is shown here for guidance regarding its form and content.)

The *Fermi* LAT Collaboration acknowledges generous ongoing support from a number of agencies and institutes that have supported both the development and the operation of the LAT as well as scientific data analysis. These include the National Aeronautics and Space Administration and the Department of Energy in the United States, the Commissariat à l'Energie Atomique and the Centre National de la Recherche Scientifique/Institut National de Physique Nucléaire et de Physique des Particules in France, the Agenzia Spaziale Italiana and the Istituto Nazionale di Fisica Nucleare in Italy, the Ministry of Education, Culture, Sports, Science, and Technology (MEXT), High Energy Accelerator Research Organization (KEK) and Japan Aerospace Exploration Agency (JAXA) in Japan, and the K. A. Wallenberg Foundation, the Swedish Research Council, and the Swedish National Space Board in Sweden.

Additional support for science analysis during the operations phase is gratefully acknowledged from the Istituto Nazionale di Astrofisica in Italy and the Centre National d'Etudes Spatiales in France.

S.C. acknowledges funding by grant ASI-INAF n.I/047/8/0 related to *Fermi* on orbit activities.

The *Fermi* LAT Collaboration extend thanks to the anonymous referee who made useful and constructive comments.

Facilities: *Fermi* (LAT).

APPENDIX

Data appearing in the plots of Figures 1 and 2 are available in Table 3.

REFERENCES

Abdo, A. A., et al. 2009a, ApJ, 700, 597
Abdo, A. A., et al. 2009b, ApJS, 183, 46
Abdo, A. A., et al. 2009c, ApJ, 699, 817
Abdo, A. A., et al. 2009d, Astropart. Phys., 32, 193
Abdo, A. A., et al. 2010a, ApJS, 188, 405
Abdo, A. A., et al. 2010b, ApJ, 710, 1271
Abdo, A. A., et al. 2010c, ApJ, 716, 30
Abdo, A. A., et al. 2010d, ApJ, 710, 810
Abdo, A. A., et al. 2010e, ApJ, 715, 429
Abdo, A. A., et al. 2010f, ApJ, 714, L73
Abdo, A. A., et al. 2010g, Nature, 463, 919
Abdo, A. A., et al. 2010h, ApJ, 713, 154
Abdo, A. A., et al. 2010i, ApJ, in press (PKS 1510-08)
Aharonian, F., et al. 2007, ApJ, 664, L71
Aller, M. F., Aller, H. D., Hughes, P. A., & Latimer, G. E. 1999, ApJ, 512, 601
Atwood, W. B., et al. 2009, ApJ, 697, 1071
Böttcher, M., & Dermer, C. D. 2010, ApJ, 711, 445
Chatterjee, R., et al. 2008, ApJ, 689, 79
Ciaramella, A., et al. 2004, A&A, 419, 485
Ciprini, S., et al. 2007, A&A, 467, 465
Dermer, C. D. 2007, ApJ, 659, 958
Edelson, R. A., & Krolik, J. H. 1988, ApJ, 333, 646
Edelson, R., Turner, T. J., Pounds, K., Vaughan, S., Markowitz, A., Marshall, H., Dobbie, P., & Warwick, R. 2002, ApJ, 568, 610
Eldar, A., & Levinson, A. 2000, MNRAS, 314, 641
Emmanoulopoulos, D., McHardy, I. M., & Uttley, P. 2010, MNRAS, 404, 931
Fiorucci, M., Marchili, N., Tosti, G., Ciprini, S., Marcucci, F., & Tramacere, A. 2003, in ASP Conf. Proc. 299, High Energy Blazar Astronomy, ed. Leo O. Takalo & E. Valtaoja (San Francisco, CA: ASP), 217
Green, A. R., McHardy, I. M., & Lehto, H. J. 1993, MNRAS, 265, 664
Hartman, R. C., et al. 2001, ApJ, 553, 683
Heidt, J., & Wagner, S. J. 1996, A&A, 305, 42
Hovatta, T., Tornikoski, M., Lainela, M., Lehto, H. J., Valtaoja, E., Torniainen, I., Aller, M. F., & Aller, H. D. 2007, A&A, 469, 899
Hovatta, T., Valtaoja, E., Tornikoski, M., & Lähteenmäki, A. 2009, A&A, 494, 527
Hufnagel, B. R., & Bregman, J. N. 1992, ApJ, 386, 473
Hughes, P. A., Aller, H. D., & Aller, M. F. 1992, ApJ, 396, 469
Komatsu, E., et al. 2009, ApJS, 180, 330
Lainela, M., & Valtaoja, E. 1993, ApJ, 416, 485
Lawrence, A., & Papadakis, I. 1993, ApJ, 414, 85
Markowitz, A. 2006, in ASP Conf. Proc. 350, Blazar Variability Workshop II: Entering the GLAST Era, ed. H. R. Miller, K. Marshall, J. R. Webb, & M. F. Aller (San Francisco, CA: ASP), 51
Marscher, A. P., et al. 2010, ApJ, 710, L126
Mastichiadis, A., & Kirk, J. G. 1997, A&A, 320, 19
Mattox, J. R., et al. 1996, ApJ, 461, 396
McHardy, I. 2008, in Proc. of Blazar Variability Across the Electromagnetic Spectrum, PoS(BLAZARS2008), 014 (http://pos.sissa.it/cgi-bin/reader/conf.cgi?confid=63)
Nandra, K., George, I. M., Mushotzky, R. F., Turner, T. J., & Yaqoob, T. 1997, ApJ, 476, 70
Nieppola, E., Hovatta, T., Tornikoski, M., Valtaoja, E., Aller, M. F., & Aller, H. D. 2009, AJ, 137, 5022
Nolan, P. L., Tompkins, W. F., Grenier, I. A., & Michelson, P. F. 2003, ApJ, 597, 615
Norris, J. P., Bonnell, J. T., Kazanas, D., Scargle, J. D., Hakkila, J., & Giblin, T. W. 2005, ApJ, 627, 324
Norris, J. P., Marani, G. F., & Bonnell, J. T. 2000, ApJ, 534, 248
Padovani, P., & Giommi, P. 1995, ApJ, 444, 567
Paltani, S., Courvoisier, T. J.-L., Blecha, A., & Bratschi, P. 1997, A&A, 327, 539
Savolainen, T., Homan, D. C., Hovatta, T., Kadler, M., Kovalev, Y. Y., Lister, M. L., Ros, E., & Zensus, J. A. 2010, A&A, 512, A24
Sikora, M., Błażejowski, M., Begelman, M. C., & Moderski, R. 2001, ApJ, 554, 1
Simonetti, J. H., Cordes, J. M., & Heeschen, D. S. 1985, ApJ, 296, 46
Smith, A. G., Nair, A. D., Leacock, R. J., & Clements, S. D. 1993, AJ, 105, 437
Sokolov, A., Marscher, A. P., & McHardy, I. M. 2004, ApJ, 613, 725
Spada, M., Ghisellini, G., Lazzati, D., & Celotti, A. 2001, MNRAS, 325, 1559
Strong, A. W., Moskalenko, I. V., & Reimer, O. 2004a, ApJ, 613, 962
Strong, A. W., Moskalenko, I. V., Reimer, O., Digel, S., & Diehl, R. 2004b, A&A, 422, L47
Takahashi, T., et al. 2000, ApJ, 542, L105
Tanihata, C., Urry, C. M., Takahashi, T., Kataoka, J., Wagner, S. J., Madejski, G. M., Tashiro, M., & Kouda, M. 2001, ApJ, 563, 569
Tavecchio, F., Ghisellini, G., Bonnoli, G., & Ghirlanda, G. 2010, MNRAS, 405, L94
Thompson, D.J. 2006, in ASP Conf. Ser. 350, Blazar Variability Workshop II: Entering the GLAST Era, ed. H. R. Miller, K. Marshall, J. R. Webb, & M. F. Aller (San Francisco, CA: ASP), 113
Ulrich, M.-H., Maraschi, L., & Urry, C. M. 1997, ARA&A, 35, 445
Valtaoja, E., Lähteenmäki, A., Teräsranta, H., & Lainela, M. 1999, ApJS, 120, 95
Vaughan, S., Edelson, R., Warwick, R. S., & Uttley, P. 2003, MNRAS, 345, 1271
Vetere, L., Massaro, E., Costa, E., Soffitta, P., & Ventura, G. 2006, A&A, 447, 499
von Montigny, C., et al. 1995, ApJ, 440, 525
Wallace, P. M., Griffis, N. J., Bertsch, D. L., Hartman, R. C., Thompson, D. J., Kniffen, D. A., & Bloom, S. D. 2000, ApJ, 540, 184
Webb, J. R. 2006, in ASP Conf. Ser. 350, Blazar Variability Workshop II: Entering the GLAST Era, ed. H. R. Miller, K. Marshall, J. R. Webb, & M. F. Aller (San Francisco, CA: ASP), 3
Webb, W., & Malkan, M. 2000, ApJ, 540, 652
Wold, M., Brotherton, M. S., & Shang, Z. 2007, MNRAS, 375, 989